

Entropy Driven Winds: Outflows and Fountains Lifted Gently by Buoyancy

Benjamin W. Keller^{1*}, J. M. Diederik Kruijssen¹, James W. Wadsley²

¹*Astronomisches Rechen-Institut, Zentrum für Astronomie der Universität Heidelberg, Mönchhofstraße 12-14, D-69120 Heidelberg, Germany*

²*Department of Physics and Astronomy, McMaster University, Hamilton, Ontario, L8S 4M1, Canada*

7 February 2020

ABSTRACT

We present a new theoretical framework for using entropy to understand how outflows driven by supernovae are launched from disc galaxies: via continuous, buoyant acceleration through the circumgalactic medium (CGM). When young star clusters detonate supernovae in the interstellar medium (ISM) of a galaxy, they generate hot, diffuse bubbles that push on the surrounding ISM and evaporate that ISM into their interiors. As these bubbles reach the scale height of the ISM, they break out of the disc, rising into the CGM. Once these bubbles break out, if they have sufficiently high entropy, they will feel an upward acceleration, owing to a local buoyant force. This upward force will accelerate these bubbles, driving them to high galactocentric radii, keeping them in the CGM for $> \text{Gyr}$, even if their initial velocity is much lower than the local escape velocity. We derive an equation of motion for these entropy-driven winds that connects the ISM properties, halo mass, and CGM profile of galaxies to the ultimate evolution of feedback-driven winds. We explore the parameter space of these equations, and show how this novel framework can explain both self-consistent simulations of star formation and galactic outflows as well as the new wealth of observations of CGM kinematics. We show that these entropy-driven winds can produce long wind recycling times, while still carrying a significant amount of mass. Comparisons to simulations and observations show entropy-driven winds convincingly explain the kinematics of galactic outflows.

Key words: – galaxies:formation – galaxies:evolution – galaxies:ISM – conduction – cosmology:theory

1 INTRODUCTION

To zeroth-order, galaxy formation is an accretion process. Dark matter (DM) haloes condense from the growth of small initial overdensities, whose distant counterparts are observable in the cosmic microwave background radiation (Press & Schechter 1974; Planck Collaboration et al. 2014). Baryons trace this structure, accreting onto DM haloes where they can cool and condense (Spitzer 1956; Rees & Ostriker 1977; Fall & Efstathiou 1980), eventually falling to the centre of the halo where they build up an interstellar medium (ISM) from which stars may form. This simple picture, however, presents us with a number of observational and theoretical problems. For one, significantly less than the expected amount of baryons are found within galaxies (Papastergis et al. 2012). Not only are there too few baryons, the fraction of these baryons that can be

found in stars is small ($< 30\%$), and this fraction has a non-monotonic relationship to the mass of the halo, peaking for halo masses of $\sim 10^{12} M_{\odot}$ (Behroozi et al. 2013; Moster et al. 2013). Despite the low star formation efficiency seen in galaxies, the metallicity of their stellar populations and ISM is even lower than what their stellar masses should have produced (Peeples et al. 2014), while observations of the circumgalactic medium (CGM) that surrounds these galaxies have found absorption lines for metals $> 100 \text{ kpc}$ beyond the star forming ISM (Aguirre et al. 2001; Martin et al. 2002). Not only are metals found well beyond the stars that created them, but modern surveys of the CGM surrounding L_{*} galaxies have found ubiquitous cool $T \sim 10^4 \text{ K}$ gas (Morganti et al. 2003; Steidel et al. 2010), which cannot be in pressure equilibrium with the volume filling hot $T \sim 10^6 \text{ K}$ CGM (Putman et al. 2012). All of these problems point towards a single potential solution: galaxies not only accrete gas, they eject it as well. Outflows driven by stellar feedback (Larson 1974; Keller et al.

* Email: benjamin.keller ‘at’ uni-heidelberg.de

2015), active galactic nuclei (AGN) (Di Matteo et al. 2005; Keller et al. 2016), radiation (Murray et al. 2011), or cosmic rays (Ipavich 1975) can all act to remove gas from the disc of a galaxy, dropping the baryon fraction, starving the star formation process, and polluting the CGM with metals and cold, entrained gas. How these outflows are launched, and the trajectory they take through the galactic corona is one of the most important unsolved problems in modern galaxy formation theory. In this paper, we present a novel framework that helps explain not only how stellar feedback can launch galactic outflows, but why these outflows are so effective at removing mass and metals from the ISM of galaxies at or below the mass of our own.

1.1 Direct and Indirect Evidence for Galactic Outflows

The retention fraction of a galaxy’s baryon budget (which totals $M_{\text{bary}} = f_B M_{\text{vir}} \sim 0.16 M_{\text{vir}}$, Planck Collaboration et al. 2014) varies for galaxies in different mass regimes, but for L_* galaxies like our own, with $M_{\text{vir}} \sim 10^{12} M_\odot$, typically 5 – 30% of the baryon budget is found in stars, and a comparable amount within the disc ISM. This leaves roughly half of the baryons unaccounted for by the components in the galactic disc, the so-called “missing baryon” problem (Fukugita et al. 1998; Cen & Ostriker 1999; Papastergis et al. 2012). Three possible solutions are that the remaining baryons are either residing within the CGM, have been expelled from the galaxy altogether, or never accreted onto the disc to begin with (White & Rees 1978). Evidence from simulations points towards most of the baryons accreted by a halo remaining in the CGM, rather than being ejected much beyond the virial radius (Muratov et al. 2015; Christensen et al. 2016; Keller et al. 2016). Recent high signal-to-noise observations of the X-ray absorption due to OVII suggest that the majority of these cosmological “missing” baryons are indeed in a warm/hot medium with $T \sim 10^6$ K surrounding galaxy overdensities (Gupta et al. 2012; Nicastro et al. 2018).

An even clearer sign of significant mass transport by galactic outflows is the presence of metals in the CGM and IGM (Songaila & Cowie 1996; Aguirre et al. 2001), combined with a relative lack of metals within the ISM and stars of galactic discs (Bouché et al. 2007; Peebles & Shankar 2011; Peebles et al. 2014). Unlike the simple deficiency of baryons that census studies like Fukugita et al. (1998); Papastergis et al. (2012) detect, so-called preventive feedback (White & Rees 1978) cannot explain this missing metal problem, as these metals were not accreted on to the disc, but formed within it. Only by ejecting them through galactic outflows can these observations be explained (Davé et al. 1998; Finlator & Davé 2008; Shen et al. 2010).

A far less simple sign of (but perhaps more subtle diagnostic for) galactic outflows is the relation between the stellar content of a galaxy and its halo mass. From the free-fall time of gas in spiral galaxies, we would expect that the vast majority of baryons would have formed stars within $\ll t_{\text{Hubble}}$, and yet we find no more than $\sim 5\%$ of the total mass of galaxies in stars in even the most massive haloes (Behroozi et al. 2013; Moster et al. 2013). A low star formation efficiency may be explained by purely intragalactic processes, such as the disruption of molecular clouds

(Murray et al. 2010; Walch et al. 2012) or the injection of turbulence (Larson 1981; Joung & Mac Low 2006). They may also be explained by purely extragalactic processes, such as inefficient cooling of the CGM (Rees & Ostriker 1977). However, most three-dimensional hydrodynamic simulations of galaxy formation find that galaxies both above (Scannapieco et al. 2012; Munshi et al. 2013) and below (Governato et al. 2004; Pontzen & Governato 2012) L_* suffer from catastrophic overcooling and runaway star formation without some form of strong, ejective feedback powering galactic outflows and winds (Hopkins et al. 2012; Keller et al. 2015). The ubiquitous failure of L_* galaxy simulations to regulate their star formation revealed by Scannapieco et al. (2012), combined with the abundance matching evidence for baryon reduction from Behroozi et al. (2013) and Moster et al. (2013) made clear that the ability for stellar feedback to drive outflows is critical to galaxy formation.

1.2 Galactic Outflows in Simulations and Semi-Analytic Modelling

With all of the previous evidence for the important role outflows play, it is unsurprising that feedback-driven outflows are important components of both semi-analytic models (Somerville & Primack 1999; Bertone et al. 2007) as well as hydrodynamic simulations (Springel & Hernquist 2003; Dalla Vecchia & Schaye 2008; Oppenheimer & Davé 2008) of galaxy evolution. Until recently, both of these methods required phenomenological descriptions of how outflows actually were launched from the ISM and travelled through the CGM. The most simple (and common) of these models assume a simple functional form for the mass outflow rates, and velocities (Springel & Hernquist 2003; Bertone et al. 2007; Oppenheimer & Davé 2008). These are often coupled to each other through a mass loading factor η , such that for a given outflow velocity v_{wind} , $\frac{1}{2}\eta v_{\text{wind}}^2 \sim 10^{49}$ erg/ M_\odot , roughly the specific energy injection available due to supernovae (Leitherer et al. 1999). In order to vary the effectiveness of these outflows in different halo scales, the functional form of η and v_{wind} often take into account the halo mass (Bertone et al. 2007), the gravitational potential (Oppenheimer & Davé 2008), or even the stellar mass (Davé et al. 2016). Typically, fairly large ($\gg 200$ km s $^{-1}$) values are chosen for the outflow velocities v_{wind} , in order to ensure that the winds can actually remove material from the ISM (or in the case where $v_{\text{wind}} > v_{\text{esc}}$, from the halo entirely, e.g. Bertone et al. 2007). The effectiveness of winds are often furthermore enhanced by decoupling them from the hydrodynamic solver (Springel & Hernquist 2003; Oppenheimer & Davé 2008; Davé et al. 2016), thereby artificially suppressing drag (which may be numerically enhanced due to poor resolution). Thus, these outflows evolve *ballistically*: with a large initial velocity, imparted directly while in the ISM, followed by an orbit through the halo unimpeded by drag (until hydrodynamic forces are re-enabled).

It has now become possible, with the advent of better numerical techniques and more powerful computing hardware to simulate galactic winds in a more self-consistent fashion. Much numerical work has gone into avoiding issues that occur when feedback is deposited into regions with in-

sufficient resolution, losing its thermal energy to numerical overcooling (Dalla Vecchia & Schaye 2012; Hopkins et al. 2014; Keller et al. 2014). These models allow for gas to be directly heated by SN, and subsequently accelerated due to either hydrodynamic forces (Dalla Vecchia & Schaye 2012; Keller et al. 2014), or due to momentum imparted by the SN ejecta (Agertz et al. 2013; Hopkins et al. 2014). The winds driven from these galaxies have been found to roughly agree with observed properties (Keller et al. 2015; Muratov et al. 2015; van de Voort et al. 2016), and appear to be successful (in some cases at least) in producing realistic disc galaxies (Hopkins et al. 2014; Crain et al. 2015; Keller et al. 2016). Unlike the simple ballistically driven, phenomenological models of galactic winds, the origin of scaling relations observed in these self-consistent models is not obvious. Wind models with imposed scalings also feature multiple free parameters, some of which may even be non-local (such as halo mass). This makes for a large volume of parameter space which must be explored through trial and error to stumble upon parameters that can yield realistic galaxies. In general, high mass loadings are seen in smaller, high redshift objects (Keller et al. 2015; Muratov et al. 2015), but how this relationship arises is unclear. High resolution simulations of wind launching sites rarely see sufficiently high velocities to escape the galactic halo, or even rise to particularly large radii (Girichidis et al. 2016; Li et al. 2017). Indeed, most cosmological simulations rarely see outflows travelling fast enough to leave the halo (Muratov et al. 2015; Christensen et al. 2016; van de Voort et al. 2016), yet they are seen to persist in the CGM for much longer than would be expected from simple ballistic recycling (Christensen et al. 2016).

1.3 Structure and Kinematics of the CGM

Recent observations have begun to reveal that the CGM is a multiphase, non-equilibrium environment (Stocke et al. 2013; Werk et al. 2014). One of the most important of these studies is the COS-Halos survey (Werk et al. 2014). By observing UV absorption in the haloes of 44 galaxies, from $L \sim 0.1L_* - 3L_*$ out 160 kpc at fairly low redshift ($z \sim 0.2$), COS-Halos has provided constraints on the temperature, density, metallicity, and kinematic state of the typical L_* CGM. COS-Halos has revealed that there is a ubiquitous, multiphase medium surrounding galaxies with a density profile for cool gas of $n_H \propto (R/R_{vir})^{-0.8 \pm 0.3}$ (Werk et al. 2014), containing a mixture of cool ($T \sim 10^4$ K) and warm ($T > 10^5$ K) gas that is out of hydrostatic equilibrium (Werk et al. 2014, 2016), and should rain out of the CGM on relatively short timescales. This material accounts for at least half of the missing baryons from L_* haloes (Werk et al. 2014; Prochaska et al. 2017), and similar fractions for the missing metals (Peeples et al. 2014; Prochaska et al. 2017). One of the most puzzling results from COS-Halos is that despite the failure of single or multiphase hydrostatic models to fit the observed density and velocity profiles (Werk et al. 2014), the velocities of the warm component is fairly slow, with $\Delta v \sim 100 - 200 \text{ km s}^{-1}$ (Werk et al. 2016), well below the escape velocities of the systems observed. For one, this warm material should be very fast if in fact the cool gas (which has similar velocities to this, see Stocke et al. 2013) has been entrained in a hot wind. For another matter, if this

material is moving well below the escape velocity, it should re-accrete on very short timescales, implying that the galactic winds are ineffective at removing material from the ISM of galaxies. Reconciling this with the low metal content and star formation efficiency seen in observations, together with the results of numerical simulations is a major problem for ballistically evolving, energy or momentum driven winds.

If we are to understand the evolution of outflows, it is important to not just understand the mechanism that powers these outflows, but the environment through which they travel. We now know that the CGM contains a significant amount of material, and that outflows ejected from the galaxy must interact with this material as they travel. For a given Lagrangian parcel of outflowing fluid, it will spend the majority of its life cycle in contact with the hot, volume-filling component of the CGM. It is therefore important to know what the volume filling, hot phase of the CGM looks like in order to calculate the effects of two critical, often ignored effects: buoyancy and drag. Buoyancy is the force which drives the convective instability, and occurs when a parcel of fluid sees an entropy gradient ∇S which points in the opposite direction to the gravitational gradient $\nabla \phi$ (Chandrasekhar 1961), and depends primarily on the entropy profile of the CGM. Drag is the loss of momentum to the surrounding fluid, and depends on both the density profile of the CGM and the cross-sectional area and velocity of the outflowing fluid. In the limit of a perfect vacuum surrounding galaxies, these effects vanish, and outflows evolve ballistically. However, COS-Halos and other studies (Steidel et al. 2010; Gupta et al. 2012; Putman et al. 2012; Stocke et al. 2013) reveal that the CGM contains significant mass, and this mass will interact with outflowing material, either imparting it with (through buoyancy or gravity) or robbing it of momentum (through drag).

The entropy profiles of massive $> 10^{13} M_\odot$ haloes have been well-studied, as their virial temperatures are large enough to make them detectable (and mappable) through their x-ray emission (Spitzer 1956; Cowie et al. 1980; Kaiser 1991). X-ray observations allows the mapping of both both the surface density and temperature of their CGM. These studies suggest that entropy profile can be fit by a simple power law. The index of this power law was first predicted by Kaiser (1991), with an index of $\alpha \sim 1.1$. Observations have confirmed the rough picture of a power law $K \propto r^\alpha$ with a $\alpha \sim 0.9 - 1.5$ slope (Werner et al. 2012; Babyk et al. 2018). Meanwhile, the density of the volume-filling phase has been mostly found to follow a power law $\rho \propto r^{-\beta}$ with slope $\beta \sim 1 - 2$ (Werk et al. 2016; Bregman et al. 2018), which, as we show in section 2.4 of this paper, is consistent with a hot halo with entropy slope of $\alpha \sim 1.1$ in hydrostatic equilibrium. Within these massive haloes, phenomena such as cooling flows (Cowie et al. 1980), buoyant AGN bubbles (Sanders et al. 2005), and the formation of stable entropy profiles and cores (Babyk et al. 2018) have all been observed. In these more massive systems, cooling times tend to be relatively long ($\sim \text{Gyr}$), while Mach numbers are small, allowing much of the halo evolution to be simplified to adiabatic, incompressible hydrodynamic interactions. The evolution of overdensities within this medium has been of primary concern. These overdensities can be subject to thermal (Nulsen 1986; Balbus & Soker 1989) and convective (Loewenstein 1989; McNamara & Nulsen 2007) instabilities, driving ma-

terial down to the center of the halo where it can fuel star formation and fuel AGN. These AGN can then in turn heat the halo gas, driving either suppressing these instabilities (Nulsen 1986; McNamara & Nulsen 2007) or driving them towards a self-regulated equilibrium (Voit et al. 2017). The recent work by Voit et al. (2017) nicely summarizes much of this theoretical work, and develops an analytic framework for understanding the interaction between AGN-driven outflows and convective/thermal instabilities in the CGM.

1.4 Entropy Driven Winds: Connecting the ISM, CGM, and Outflows

In simulations that allow winds, fountains, and outflows to be launched self-consistently (Muratov et al. 2015; Keller et al. 2016; Agertz et al. 2013), understanding the behaviour of these outflows, and how they scale with various galaxy properties is difficult. It is clear that the state of the ISM as well as the properties of the galaxy halo and hot CGM all play a role in setting the mass loadings, recycling times, and velocities of outflows. In particular, we have found in Keller et al. (2015, 2016) that the effectiveness of supernovae-driven winds falls precipitously once the halo mass exceeds $10^{12} M_{\odot}$. Understanding this behaviour requires a theory that takes into account gravity as well as hydrodynamic effects from the ISM and CGM, that can explain the typical observed kinematics (Werk et al. 2014), as well as the relatively long re-accretion times for mass-loaded winds seen in simulations (Keller et al. 2015; Christensen et al. 2016; Muratov et al. 2015).

In this paper, we present a new model for understanding the flows of material out of the galaxy. Building on previous studies that developed the theory of convective and thermal instability in the haloes of massive galaxies, as well as analytic models for superbubbles driven by clustered supernovae, we show how buoyancy can drive outflows to high galactic radii in Milky Way like L_* galaxies. Accelerated gently through the CGM, rather than ballistically from within the ISM, entropy driven fountains can have recycling times of $> \text{Gyr}$ without reducing their mass loading. We also examine how buoyancy and radiative cooling sets important limits on the effectiveness of supernovae feedback in haloes more massive than $10^{12} M_{\odot}$, and when the gaseous disc is dense and thin. Finally, we compare the behaviour of entropy-driven outflows to cosmological galaxy and high-resolution ISM simulations, as well as observations of gas flows within the CGM.

2 DERIVING THE EVOLUTION OF ENTROPY DRIVEN WINDS

2.1 CGM Entropy

In most studies of hot coronae around galaxies (Cowie et al. 1980; Voit et al. 2017), the thermodynamic entropy S is replaced with the more easily-measured and expressed adiabatic invariant K , defined simply using the temperature T and number density n of a parcel of fluid:

$$K = k_B T n^{1-\gamma} \quad (1)$$

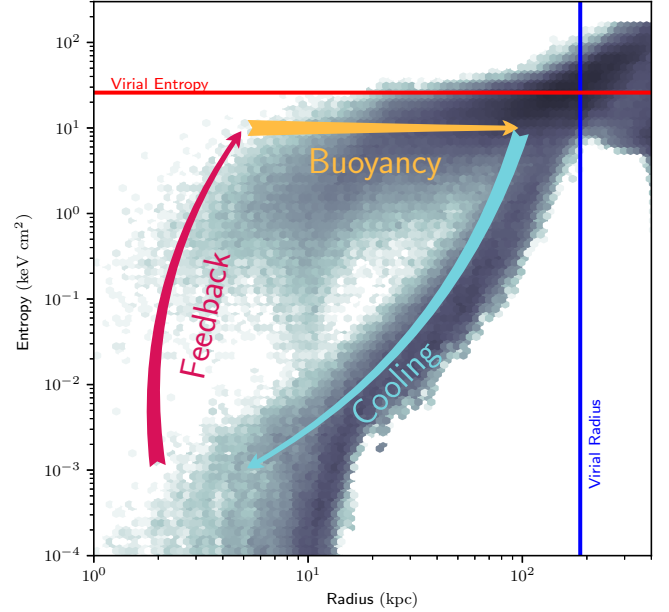


Figure 1. The flow of gas through the CGM in the entropy-driven wind framework. Feedback drives gas to high entropies within the ISM, which then break out of the disc and rise buoyantly, conserving their entropy as they expand adiabatically. Eventually, the temperature of feedback heated gas drops to the peak of the cooling curve at $\sim 10^5 \text{K}$. The gas can then lose entropy, and thus become negatively buoyant. This allows it to accrete back upon the disc, and potentially continue the cycle once more. The background histogram shows gas particles from the MUGS2 galaxy g1536.

This is related to the specific Clausius entropy S (for a fluid with specific isochoric heat capacity c_V) simply as:

$$S = c_V \ln K \quad (2)$$

While, formally, K is not the true thermodynamic entropy, we will follow the convention of referring to this as “entropy” for the remainder of this paper.

From this simple definition, we can derive for a halo a “virial entropy”, the entropy of a virialized halo at the virial radius R_{200} . If the virial radius is defined as the radius within which a M_{200} halo has average density $\rho_{200} = 200\rho_{crit}$:

$$R_{200} = \left(\frac{4}{3} \pi (\rho_{200}) \right)^{-1/3} M_{200}^{1/3} \quad (3)$$

Gas at this radius has a characteristic virial temperature T_{200} , such that the gas has thermal/kinetic energy equal to half the gravitational potential energy of the halo:

$$T_{200} = \frac{2GM_{200}}{3R_{200}} \frac{\mu m_p}{k_B} \quad (4)$$

Together, equations 3 and 4 can be used to derive a virial temperature for a halo of mass M_{200} :

$$T_{200} = \frac{G\mu m_p}{k_B} \left(\frac{4\pi\rho_{200}M_{200}^2}{27} \right)^{1/3} \quad (5)$$

Therefore, when we define using equation 1 our virial en-

tropy K_{200}

$$K_{200} = k_B T_{200} \left(\frac{f_B \rho_{200}}{\mu m_p} \right)^{1-\gamma} \quad (6)$$

where f_B is the baryonic mass fraction of the halo. We shall use a value of $f_B = 0.16$ for this study. We can use equation 5 to derive an expression for the virial entropy for a halo of mass M_{200} , given an adiabatic index of $\gamma = 5/3$:

$$K_{200} = G \left(\frac{f_B^2 \pi \mu^5 m_p^5 M_{200}^2}{150 \rho_{crit}} \right)^{1/3} \quad (7)$$

In units of keV cm^2 , this gives the simple relation for ionized gas with solar metallicity (and thus a mean molecular weight of $\mu = 0.62$):

$$K_{200} = 30.06 \text{ keV cm}^2 \left(\frac{M_{200}}{10^{12} M_\odot} \right)^{2/3} \quad (8)$$

For the rest of this paper, we will continue using an adiabatic index of $\gamma = 5/3$ and a mean molecular weight of $\mu = 0.62$.

2.2 Superbubble Entropy

We can also estimate the entropy generated in feedback-heated superbubbles. Following calculations from Weaver et al. (1977) and Mac Low & McCray (1988), we can calculate the interior density of the superbubble at time $t_7 = t/10$ Myr, driven by a luminosity of $L_{38} = L/10^{38} \text{ erg s}^{-1}$ in an ambient medium of density $n_{amb} (\text{cm}^{-3})$, as a function of the distance r from the centre of a superbubble of radius R_{SB} :

$$n(r) = 4 \times 10^{-3} \text{ cm}^{-3} L_{38}^{6/35} n_{amb}^{19/35} t_7^{-22/35} (1-r/R_{SB})^{-2/5} \quad (9)$$

Integrating this equation from 0 to R_{SB} , we find the total mass contained within the bubble is:

$$m_{SB} = \frac{125}{39} \pi \mu m_p n(0) R_{SB}^3 \quad (10)$$

In the limit of weak cooling, the partition of energy in a luminosity-driven bubble gives the internal energy of $U = 5/11 Lt$. The mean temperature of the bubble interior is therefore given as:

$$T = \frac{26}{275 k_B \pi} n(0)^{-1} R_{SB}^{-3} Lt \quad (11)$$

We assume during the superbubble break out process, the interior becomes well-mixed. This allows us to apply the Kompaneets (1960) approximation to the hot bubble's density as well as pressure, and this equation and the average density of the superbubble to determine the entropy of out-flowing material using equation 1:

$$K_{SB} = \frac{26}{275 \pi} \left(\frac{375}{156} \right)^{-2/3} n(0)^{-5/3} R_{SB}^{-3} Lt \quad (12)$$

The break out of the superbubble-heated gas occurs when the radius of the bubble is roughly equal to the scale height of the ISM $R_{SB} \sim h$ (Kruijssen et al. 2019), so that we can take the equation for the bubble radius R_{SB} :

$$R_{SB} = 267 \text{ pc } L_{38}^{1/5} n_{amb}^{-1/5} t_7^{3/5} \quad (13)$$

and invert it to solve for t_7 with $R_{SB} = h$:

$$t_7 = \left(\frac{h}{267 \text{ pc}} \right)^{5/3} L_{38}^{-1/3} n_{amb}^{1/3} \quad (14)$$

This gives a superbubble density at breakout that scales as $n_{SB} \propto L^{8/21} h^{-22/21} n^{1/3}$. If we assume the stellar cluster driving this superbubble is a single stellar population with a Chabrier (2003)-like IMF, then $L_{38} \sim M_{cluster}/10^4 M_\odot$. Recent observations show typical young stellar clusters (YSCs) have masses in the range of $10^4 - 10^6 M_\odot$ (Longmore et al. 2014; Ginsburg et al. 2018; Mok et al. 2019). The last SNe detonates ~ 30 Myr after the birth of the cluster, and thus the assumption of a constant luminosity driving is correct so long as $t_7 < 3$. As is shown in figure 2, this is the case for a large fraction of the ISM/star cluster configuration space.

This can finally be combined with equation 12 to derive the entropy of superbubble gas as it breaks out from the ISM of a disc with scale height h .

$$K_{SB} = 5.84 \text{ keV cm}^2 \left(\frac{h}{267 \text{ pc}} \right)^{26/63} L_{38}^{2/63} n_{amb}^{-14/63} \quad (15)$$

If this hot bubble has entropy greater than the inner corona, it will experience a buoyant force upwards.

We may also calculate a maximum entropy in the case of a poorly-mixed bubble, where the most buoyant fraction of the superbubble will accelerate away from the lower-entropy edges of the bubble. In this case, we can use the equation for the peak temperature, together with equation 9:

$$T(r) = 3.5 \times 10^6 \text{ K } L_{38}^{8/35} n_{amb}^{2/35} t_7^{-6/35} (1-r/R_{SB})^{2/5} \quad (16)$$

Setting $r = 0$ in both of these equations allows us to derive a maximum superbubble entropy K_{max} :

$$K_{max} = 11.97 \text{ keV cm}^2 L_{38}^{4/35} n_{amb}^{-34/105} t_7^{26/105} \quad (17)$$

Which, together with equation 14, can derive a final value for this maximum entropy:

$$K_{max} = 11.97 \text{ keV cm}^2 \left(\frac{h}{267 \text{ pc}} \right)^{26/63} L_{38}^{2/63} n_{amb}^{-76/315} \quad (18)$$

As can be seen here, the maximum entropy is ≈ 2 times the average entropy in a superbubble venting from a typical disc galaxy. Note however the slightly stronger density dependence on the maximum entropy. Naturally, this high-entropy component will carry substantially less mass out of the galaxy, and is therefore unlikely to be an effective measure of the entropy in the heavily mass-loaded winds predicted by theory, simulations and observed in absorption line studies.

2.3 Equations of Motion for a Buoyant Bubble

Beginning with the Euler equation for momentum conservation, we can derive an equation of motion for a buoyant bubble rising through a medium in a gravitational potential ϕ :

$$\frac{D\mathbf{u}}{Dt} = \frac{\nabla P_{SB}}{\rho_{SB}} - \nabla \phi \quad (19)$$

If the sound crossing time inside the superbubble is less than the time it takes for the superbubble to cross a pressure scale length for the background CGM (Kompaneets 1960), then it will stay in pressure equilibrium with the environment, such that $P_{SB} \sim P$. As the density of the superbubble can be expressed in terms of pressure and entropy using equation 1 ($\rho = \mu m_p (P/K)^{3/5}$), we can re-write the momentum

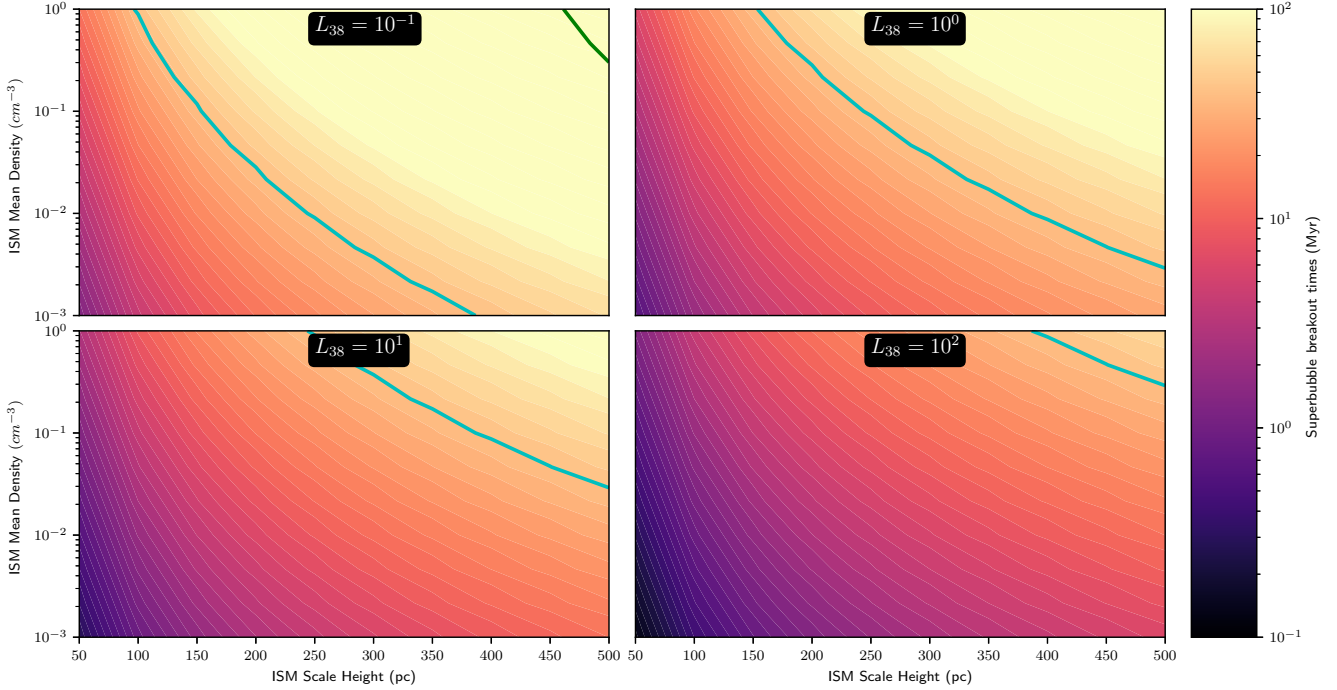


Figure 2. The break out time of a superbubble driven by four different mass star clusters, in a range of different ISM environments (mean density vs. scale height). The four panels show the break out time for a star cluster of mass $10^3 M_{\odot}$ (upper left), $10^4 M_{\odot}$ (upper right), $10^5 M_{\odot}$ (lower left), and $10^6 M_{\odot}$ (lower right). The cyan curves show break out times of 40 Myr. Regions to the right of this curve cannot break out of the disc before their SN shutoff, breaking the assumption of constant-luminosity driving. The green curve shows $0.1 t_{cool}$, the time required for the interior of the superbubble to lose 10% of its thermal energy. As is clear here, even the smallest star clusters can drive a superbubble out of the ISM before an appreciable amount of energy is lost to cooling.

equations as:

$$\frac{D\mathbf{u}}{Dt} = \frac{\nabla P}{\mu m_p P^{3/5}} K_{SB}^{3/5} - \nabla\phi = \frac{\nabla P}{\rho} \left(\frac{K_{SB}}{K} \right)^{3/5} - \nabla\phi \quad (20)$$

If the background CGM is in hydrostatic equilibrium, then $\nabla P/\rho = \nabla\phi$, and we can write an equation for the Lagrangian acceleration of the hot bubble through an entropy-stratified, hydrostatic CGM (Archimedes' principle, in entropy form):

$$\ddot{r} = \nabla\phi \left[\left(\frac{K_{SB}}{K(r)} \right)^{3/5} - 1 \right] \quad (21)$$

The first, positive term of this equation is the buoyant force due to the local entropy gradient, while the second, negative term is simply the gravitational acceleration. As is clear from this, when the superbubble entropy K_{SB} is greater than the CGM entropy $K(r)$, the bubble will feel a positive, upward buoyant acceleration. In the limit where K_{SB} goes to zero, it will experience gravitational free-fall. If our CGM entropy profile is set by a simple power-law:

$$K(r) = K_{200} \left(\frac{r}{R_{200}} \right)^{\alpha} \quad (22)$$

We can then derive an acceleration for our superbubble in terms of the virial entropy K_{200} and the bubble's entropy K_{SB} and height in the halo r , which can be simplified using the assumption of a flat rotation curve with $\nabla\phi = v_c^2/r$:

$$\ddot{r} = \frac{v_c^2}{r} \left[\left(\frac{K_{SB} R_{200}^{\alpha}}{K_{200} r^{\alpha}} \right)^{3/5} - 1 \right] \quad (23)$$

Setting the left-hand side of this equation to zero tells us that, as we might expect, the bubble ceases to be buoyant when it reaches a radius where its entropy is equal to the surrounding material (which can also be derived directly from the power-law entropy profile):

$$r_{max} = \left(\frac{K_{SB}}{K_{200}} \right)^{1/\alpha} R_{200} \quad (24)$$

2.4 Damping by Drag

When we include the effects of drag, we can derive the final set of equations governing the motion of the bubble. The fluid drag that the bubble encounters is a function of the local CGM density $\rho(r)$ and the velocity of the blob \dot{r} :

$$\ddot{r} = -\rho(r) C_D \frac{\dot{r}^3 \pi R_{SB}(r)^2}{|\dot{r}| m_{SB}} \quad (25)$$

Where C_D is the geometrically-dependent drag coefficient. For a sphere, $C_D \sim 1/2$. We note the dependence of this expression on the bubble radius R_{SB} , which thus needs to be solved for. If the CGM gas follows a power-law profile $\rho(r) = \rho_0 (r/r_0)^{-\beta}$, then we can derive a value for the bubble radius as it rises, assuming it stays in pressure equilibrium with the surrounding medium:

$$P = K n^{5/3} \propto r^{\alpha-5\beta/3} \quad (26)$$

We assume that our CGM is in hydrostatic equilibrium, with a potential set by the dark halo with negligible baryonic contribution (and assuming, as above, a flat rotation curve

with $v_c^2 = GM_{200}/R_{200}$, then we can use this to determine β :

$$\frac{dP}{dr} = -\nabla\phi\rho(r) \quad (27)$$

$$\left(\frac{5}{3}\beta - \alpha\right)K_{200}\rho_0^{2/3}r_0^{2\beta/3}r^{\alpha-2\beta/3} = \frac{GM_{200}}{R_{200}} \quad (28)$$

Solving this equation yields the density profile slope $\beta = 3\alpha/2$. We can then integrate the density equation to determine the normalization of the density profile. If we assume that f_{CGM} of the galactic baryons reside within the CGM, then:

$$\rho_0 = \frac{f_B f_{CGM} M_{200}}{4\pi R_{200}^3} (2 - 3\alpha/2) \quad (29)$$

For the bubble to stay in pressure equilibrium with the CGM as it rises, it must grow from an initial radius of $R_{SB} \sim h$ to

$$R_{SB}(r) = h^{1-3\alpha/10} r^{3\alpha/10} \quad (30)$$

This finally allows us to determine the drag acceleration:

$$\ddot{r} = \frac{-C_D f_B f_{CGM} M_{200}}{4m_{SB}} h^{1-3\alpha/10} r^{-6\alpha/5} R_{200}^{3\alpha/2-3} \frac{\dot{r}^3}{|\dot{r}|} \quad (31)$$

Combining this with equation 23, we can finally derive the full equation of motion that takes in to account the effects of buoyancy, gravity, and fluid drag on this outflowing superbubble:

$$\ddot{r} = \frac{v_c^2}{r} \left[\left(\frac{K_{SB} R_{200}^\alpha}{K_{200} r^\alpha} \right)^{3/5} - 1 \right] - \xi r^{-6\alpha/5} \frac{\dot{r}^3}{|\dot{r}|} \quad (32)$$

Where $\xi = -C_D f_B f_{CGM} M_{200} (4m_{SB})^{-1} h^{1-3\alpha/10} R_{200}^{3\alpha/2-3}$ is the constant-valued coefficient for drag set by the halo and the superbubble initial conditions. For the calculations that follow, we assume $f_{CGM} = 0.5$, roughly in agreement with the values of the CGM mass fraction observationally determined by COS-Halos (Werk et al. 2014), and the amount required to explain the so-called ‘‘missing baryons’’ (Gupta et al. 2012).

The overall picture presented here is shown in schematic form in figure 1: entropy generated by feedback lifts gas up through the CGM, on a roughly adiabatic track. Once that gas reaches its buoyant equilibrium point, it may then cool radiatively, returning back to the ISM. This cooling-feedback-buoyant uplift cycle will keep material in the CGM, regulating the star formation, baryon masses, and metal content of galaxies.

3 THE TRAJECTORY OF A BUOYANT BUBBLE IN A MILKY-WAY-LIKE CGM

We can take the equations of motion from equation 32 and integrate them forward in time numerically. We use the `scipy` wrapper (Jones et al. 2001) for the ODEPACK LSODA method, which automatically switches between an Adams-Bashforth and Backward Differentiation Formula (BDF) method when the equations pass a stiffness criterion (Hindmarsh 1982). With this, we are able to evolve the position and velocity of the buoyant wind over time.

We can start with a fairly simple case, to allow us to

see the qualitative behaviour of equation 32 integrated over time. As figure 3 shows, for a reasonably sized star cluster ($M \sim 10^4 M_\odot$) in a Milky-Way like ISM with density $n_{amb} = 1 \text{ cm}^{-3}$ a scale height of 200 pc (Dehnen & Binney 1998), the apoapsis of the bubble’s flight is actually significantly higher than the buoyant equilibrium radius in the CGM where it later oscillates about. This phenomenon is convective overshooting, occurring due to simple momentum conservation. The bubble’s oscillations subsequent to this are damped fairly heavily by drag, as is shown in figure 3. As that figure shows, these bubbles never exceed velocities of $\sim 200 \text{ km s}^{-1}$ in M_* halos, despite being ejected to $\sim 100 \text{ kpc}$ and re-accreting on timescales $> \text{Gyr}$.

If we compare this behaviour to a kinetically launched, ballistic trajectory, we see qualitatively that there is a stark difference between the two wind launching mechanisms. We calculate an initial velocity for the bubble assuming that 100% of the driving luminosity goes into kinetic energy, launching a mass given by equation 10. In order to maximize the effects of this ballistic wind, we do not include the drag terms given by equation 31, allowing the bubble to be slowed by gravity alone. We see in figure 4 that unlike entropy driven winds, these energy/momentum driven outflows initially travel fairly fast ($\sim 400 \text{ km s}^{-1}$) compared to the average in COS-Halos Werk et al. (2014). However, as this velocity is below the escape velocity for the range of halo masses we examine, this material rapidly re-accretes on timescales $\ll t_{bubble}$, and only reaches modest heights above the disc. If a sufficiently smaller mass loading is assumed, this lower mass would of course have a higher velocity. If that velocity exceeded the escape velocity of the halo, would allow the material to leave beyond the virial radius. This is a key difference between entropy driven winds and winds propelled ballistically: entropy-driven winds do not ‘‘fail’’ in the same way as ballistically driven winds. Even with their lower characteristic velocities, entropy-driven winds persist in the CGM long after ballistically propelled outflows would have re-accreted.

If we consider an arbitrary mass-loading η , then the initial velocity of this wind, assuming 100% of the energy deposited by supernovae is coupled to the kinetic energy of this outflowing material, we can see that $v_0 \sim 700\eta^{-1/2} \text{ km s}^{-1}$. For an NFW halo the escape velocity is $v_{esc} = \sqrt{6}cv_{200} \sim 800 \text{ km s}^{-1} (M_{200}/10^{12} M_\odot)^{1/3}$ (assuming a concentration of $c \sim 4$, Zhao et al. 2003). This means that for outflow mass loadings to be significant $\eta > 1$, and not re-accrete on short $\sim 100 \text{ Myr}$ timescales, these outflows cannot be driven ballistically. Entropy-driven winds, on the other hand, naturally give high mass loadings with long recycling times.

3.1 Cooling of the Hot Bubble

Radiative cooling of the hot interior of a superbubble will remove entropy from that gas. If the cooling time of the superbubble is short compared to the time it spends cycling through the CGM, it will lose buoyancy and fall back to the ISM. However, as it rises through a progressively lower-pressure CGM it will expand adiabatically, decreasing both its density and temperature. This has two opposing effects: decreasing the cooling rate due to lower density, while increasing the cooling rate as it approaches the recombination peak of the cooling curve at 10^5 K (Raymond et al. 1976).

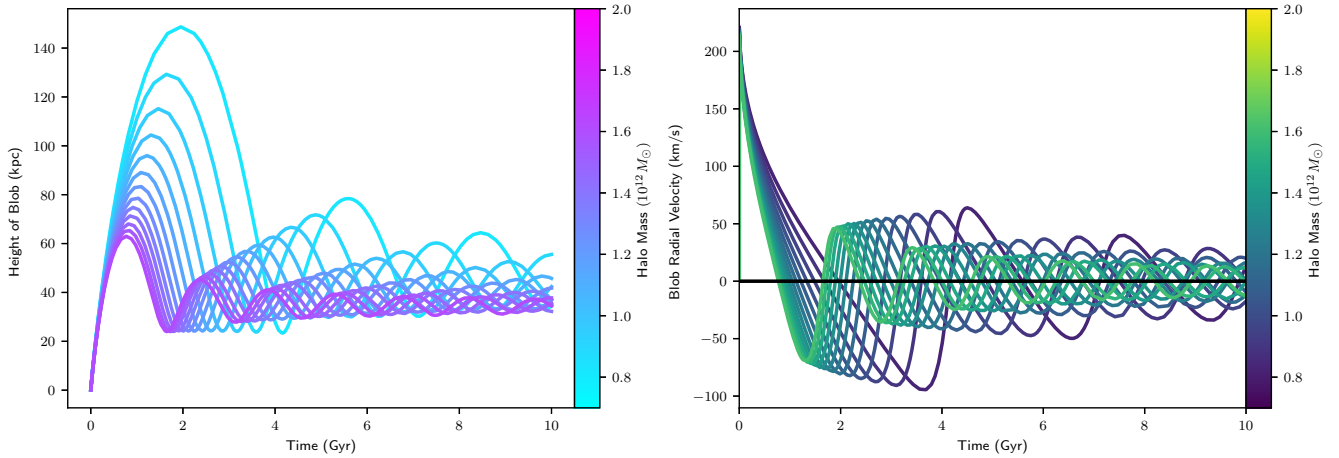


Figure 3. Flight of a buoyant bubble through the CGM. Left panel: Altitude in the galactic halo of a superbubble driven by a cluster with a mechanical luminosity of 10^{38} erg/s ($M_{cluster} 10^4 M_{\odot}$). The cluster is embedded in a Milky Way-like ISM with a HI scale height of 200 pc and an averaged ISM density of 1 cm^{-3} . The color of each curve denotes the virial mass of the galaxy. Right panel: velocity of the same bubble. As can be seen, the bubble is rapidly accelerated during the first few 100 Myr of its flight through the CGM, and then subsequently loses velocity as it convectively overshoots and is damped through drag.

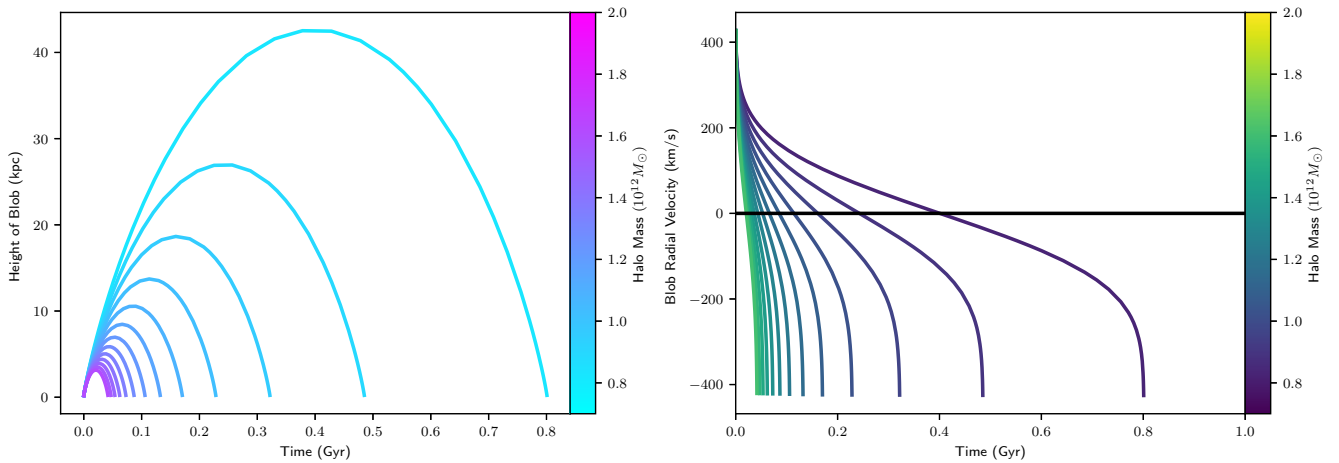


Figure 4. Flight of a ballistic bubble through the CGM. Left panel shows galactocentric radius, right panel shows bubble velocity. Note that the time range on the horizontal axis is 10 times shorter than the previous figure. If, rather than allowing the hot interior of a superbubble to rise buoyantly, it is ejected ballistically, it will re-accrete on a much shorter timescale. Here we see the trajectory of a parcel of gas assuming all of the star cluster feedback is deposited as kinetic energy into a mass set by equation 10. When buoyant uplift is unaccounted for, the fountain cycling time drops well below \sim Gyr. When a bubble is launched ballistically, it begins with a fairly high ($> 400 \text{ km s}^{-1}$) velocity, which it rapidly loses to gravity. Note that here we *do not* include the effects of drag, effectively maximizing the ability for ballistically launched outflows to escape.

Simply calculating the cooling time of the bubble at break out is insufficient to determine whether it will evolve adiabatically as it rises through the CGM.

We therefore instead use the trajectories of bubbles rising through the CGM, calculated by numerically integrating equation 21 to obtain temperatures and densities for superbubbles launched from a number of potential ISM environments. From equation 11 and equation 14, we can see that the temperature of the bubble at break out is independent of the ambient density, as $n(0) \propto n_{amb}^{1/3}$ and $t_7 \propto n_{amb}^{1/3}$, while $T \propto t_7/n(0)$. This temperature should scale weakly with scale height, $T \propto h^{-3/7}$. The density of the bubble will scale sub-linearly with ambient density, with $n_{SB} \propto n_{amb}^{1/3}$

and will be nearly linear with the inverse of the ISM scale height $n_{SB} \propto h^{-22/21}$. Since the primary cooling processes are collisional at the temperatures of this bubble, and therefore $\Lambda \propto n_{SB}^2$, this suggests that the ambient density n_{amb} is the primary parameter for determining whether the superbubble will cool, unless we approach the peak of the cooling curve, where $|\frac{d\Lambda}{dT}|$ becomes large.

In order to investigate the evolution of the cooling times with more rigour, we used the GRACKLE cooling library (Smith et al. 2017) to calculate the cooling times of the bubble at each timestep as its trajectory through the CGM is integrated. These cooling times can be compared to the timescale required for the bubble to travel signifi-

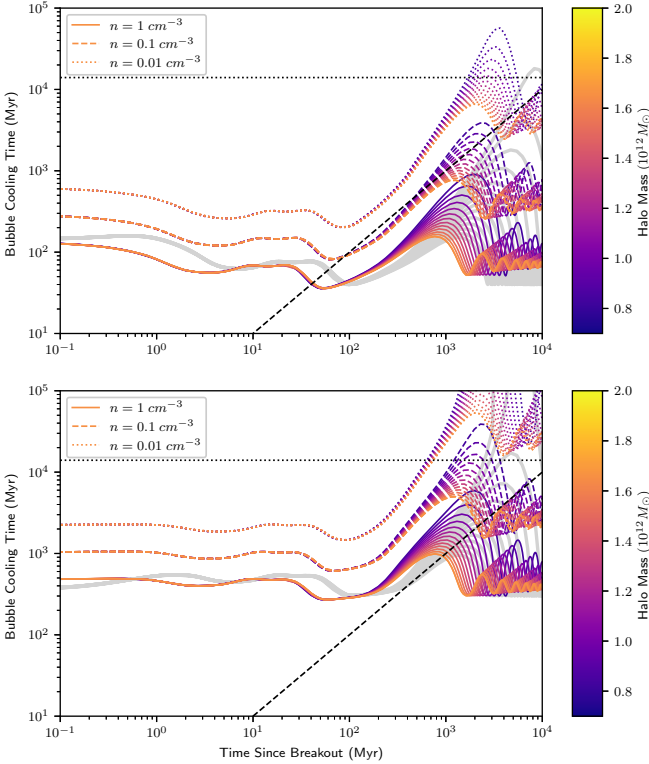


Figure 5. Cooling time of a hot bubble in as it rises through the CGM. The top panel shows the cooling times for a metallicity of Z_{\odot} , while the bottom shows cooling times for a metallicity of $0.1Z_{\odot}$. The three different line styles (solid, dashed, and dotted) show cooling times for superbubbles driven in an ISM with ambient density of 1 cm^{-3} , 10^{-1} cm^{-3} , and 10^{-2} cm^{-3} respectively. The horizontal dotted line shows a Hubble time, and the dashed black curve shows the 1 : 1 line, where the cooling time is equal to the bubble’s age, and shows roughly when the bubble will lose its entropy to radiative cooling. The light grey curves show how, paradoxically, increasing the SN luminosity of the cluster by a factor of 10 doesn’t significantly change the time when it cools. As this figure shows, pre-processing of the ISM by early feedback or past SN explosions, thus lowering the ambient density superbubbles detonate in, is essential to producing superbubbles with sufficiently long cooling times to rise through the CGM without radiating away their entropy.

cant distances from the disc, and as an estimate for the timescale over which the bubble can continue to oscillate in the CGM. We assume that each bubble has solar metallicity $Z = 0.0129$, and that it is subject to a [Haardt & Madau \(2012\)](#) UV background field. We vary the background density and ISM scale height, as well as the SN luminosity of the driving cluster. As figure 5 shows, while the initial cooling time of the bubble scales as we expect, sublinear with the ambient ISM density, the subsequent evolution, especially as the bubble reaches it’s apsis, is sensitive to both the ISM scale height and the ambient density. For metallicities below solar, however, the cooling rates are suppressed by the lack of metal emission lines, and with a reduction to just $Z = 0.1Z_{\odot}$, even clusters in a dense ISM will be able to drive bubbles that take $\sim \text{Gyr}$ to cool. This means that entropy-driven winds would have been more effective at higher red-

shift, when the cosmic metallicity was lower, and even more effective than the scalings relative to halo mass we will see with constant (solar) metallicity, as the mass-metallicity relation ([Erb et al. 2006](#); [Ma et al. 2016](#)) implies lower mass galaxies will have lower metallicities. These galaxies will thus not only have lower virial entropies, but superbubbles driven from their ISM will have longer cooling times.

3.2 How Far Can Buoyant Outflows Travel?

It is clear from the previous sections (and of course, from the derived equations) that the evolution of buoyant bubbles through the CGM has dependence on a number of factors: the radiative cooling of gas, the ISM scale height and density, the driving cluster mass/luminosity, and the mass of the halo. In this section, we explore the sensitivity of outflows to these parameters. We integrate our equation of motion, equation 21 over a 4-dimensional grid spanning $L_{38} = 0.1 - 100$, $h = 50 - 500 \text{ pc}$, $n_{amb} = 10^{-3} - 1 \text{ cm}^{-3}$, and $M_{200} = 0.7 - 2 \times 10^{12} M_{\odot}$. We also use GRACKLE to calculate cooling times for each point in our integration.

Figure 6 shows the maximum apoapsis (height) of the bubble during an integration time of 10 Gyr. This height is always the first turnover point in the flight (as subsequent oscillations are damped by drag), except in the case where the apoapsis time is $> 10 \text{ Gyr}$. A number of features are clear from these panels. First, as the virial mass increases, the maximum height obtained by the bubble is, unsurprisingly, decreased. For our lightest halo, most of the parameter space allows for a $10^4 M_{\odot}$ cluster to launch an entropy-driven outflow that will escape beyond the virial radius. Secondly, the ISM that maximizes the bubble’s apoapsis is one which is thick and diffuse, with a low ambient density and large scale height. Finally, as the mass of the cluster increases, the maximum distance the subsequent outflow can reach increases as well.

The time that these outflows reside in the CGM, more so than the distance they reach, is critical to actually regulating the star formation, black hole growth, and baryon content of the galactic disc. Only by spending a significant fraction of the galaxy’s lifetime in the CGM can entropy-driven outflows suppress star formation and bulge/black hole growth. In figure 7, we show the time that a bubble takes to reach the maximum height (this time can be thought of as $\sim 1/2$ of the re-accretion time, if we assume that the first periapsis drives the material back onto the ISM). As this figure shows, for essentially all of the configuration space we have examined, entropy-driven winds can produce outflows that take $> \text{Gyr}$ to re-accrete. This means that a parcel of fluid need only be ejected a handful of times to spend most of its life outside of the star forming disc, as opposed to the hundreds of times required for a mass-loaded, kinetically driven wind in a $2 \times 10^{12} M_{\odot}$ halo. Even when radiative cooling is considered, as long as the ambient ISM is sufficiently diffuse, either due to gas exhaustion of the natal molecular cloud ([Kruijssen et al. 2012](#); [Longmore et al. 2014](#); [Ginsburg et al. 2016](#)) or pre-treatment by early stellar feedback ([Chevance et al. 2019](#)), the bubble will still spend a significant fraction of t_{bubble} in the CGM. We show the radiative cooling times in figure 8. As this shows, there is a sharp distinction between bubbles with short ($\sim 100 \text{ Myr}$) and long ($> \text{Gyr}$) cooling times. This dividing region is sharpest in

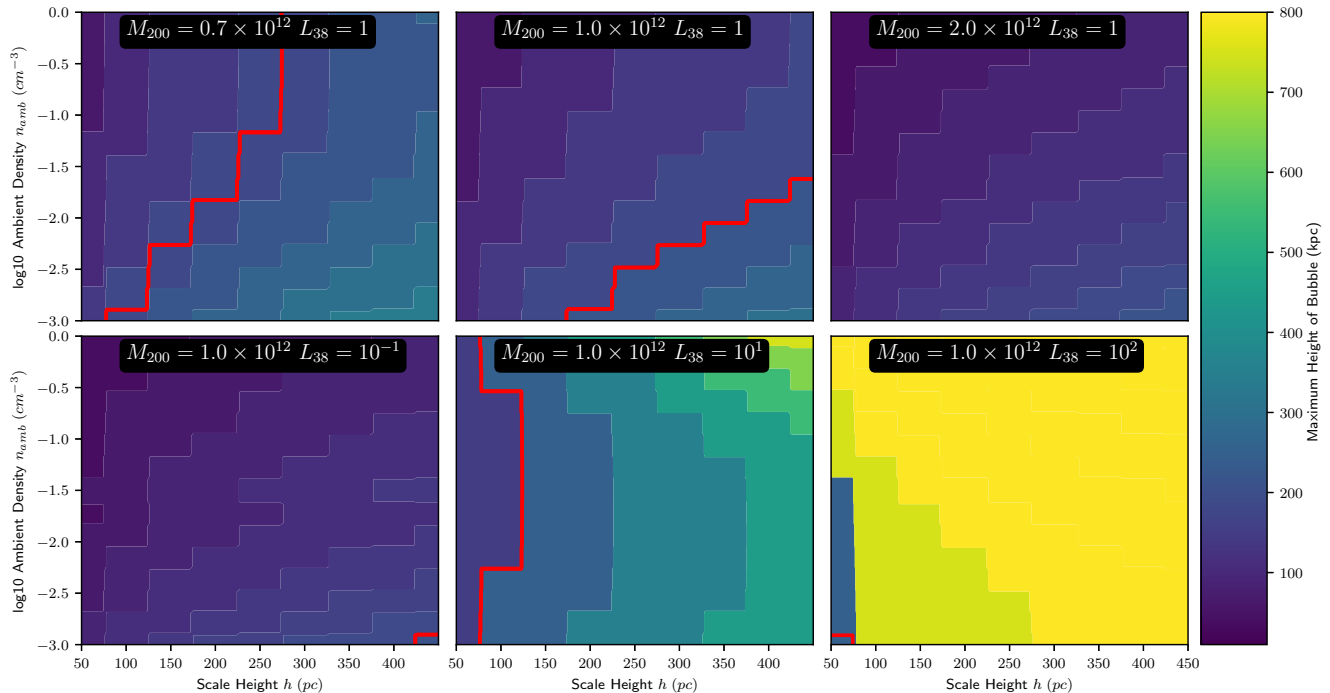


Figure 6. Contour plot of the maximum height (within the 10 Gyr of integration time we use) obtained by a buoyant bubble launched from a number of different ISM conditions, by a range of driving luminosities, for 3 different halo masses. The top row shows bubbles driven by a cluster with luminosity 10^{38} erg s $^{-1}$, for halo masses of $7 \times 10^{11} M_{\odot}$, $10^{12} M_{\odot}$, and 2×10^{12} (left to right). The bottom row shows the result of a cluster with 10^{37} erg s $^{-1}$, 10^{39} erg s $^{-1}$, and 10^{40} erg s $^{-1}$ (left to right) in a halo with $M_{200} = 10^{12} M_{\odot}$. The red contour shows the virial radius of the halo. As would be expected from equation 15, bubbles escaping from thicker, lower-density ISM reach higher through the CGM, and bubbles rising through the CGM of more massive haloes are trapped to lower heights. Even bubbles which do not reach the virial radius of their haloes still can rise ~ 100 kpc in all but the most massive haloes, with the densest, thinnest ISM. The black lines show when the bubbles have at 10 Gyr still not yet reached their highest altitude.

low-mass haloes, where the bubble reaches greater heights and experiences the largest amount of adiabatic cooling. The most important factor is not the halo mass, however, but the ambient density, and to a lesser extent, the ISM scale height. These two factors determine both the temperature and density of the bubble at break out. A more diffuse ambient medium gives a cooler, more diffuse bubble, as does a larger ISM scale height. With a diffuse enough ambient ISM, the cooling time of the bubble will be sufficient for it to both reach large apocentric distances and stay out of the star forming-ISM.

Indeed, when we look instead at the maximum height a bubble obtains while it is still evolving adiabatically, in figure 9, we can see that for our most massive halo $2 \times 10^{12} M_{\odot}$, only very large clusters, driving superbubbles in extremely diffuse, thick discs can actually drive outflows to an appreciable distance through the CGM, reaching just a few times 10 kpc before radiative losses sap them of their entropy. For a $< 10^{12} M_{\odot}$ halo, the largest star clusters can easily eject material beyond the virial radius. The somewhat stronger dependence on cluster mass (L_{38}) that we see here compared to figure 6 is due to the additional influence of radiative cooling. Without radiative losses, the relative importance of L_{38} is weaker (as we would expect from equation 15). When radiative losses are included, the higher initial SB temperature allows the bubble to retain its entropy for longer, reaching higher altitudes in the CGM. Though

the lowest mass clusters only loft material to ~ 100 kpc, figure 8 shows this material will stay held in the CGM by buoyancy for > 1 Gyr if the SB detonate in regions that have density below $n_{amb} \sim 0.1$ cm $^{-3}$. As we will see later, this is not a particularly stringent criterion.

3.3 Mass Loading and Mixing

Whether entropy-driven winds can actually remove a significant amount of mass from the galactic ISM depends critically on how much material is actually carried by the bubble. In the limit where the only mixing that occurs between the ISM and the hot bubble is the evaporation captured in equation 9, the mass loading value η is simply $\eta = m_{SB}/M_{cluster}$. We can use equation 10, along with $L_{38} \sim M_{cluster}/10^4 M_{\odot}$, to calculate this:

$$\eta = 1.18 \left(\frac{n_{amb}}{\text{cm}^{-3}} \right)^{1/3} \left(\frac{M_{cluster}}{10^4 M_{\odot}} \right)^{-13/21} \left(\frac{h}{267 \text{ pc}} \right)^{41/21} \quad (33)$$

This shows that, a more massive cluster will give lower mass loadings than a less massive one. This is simply because a more massive cluster will produce a bubble with density that scales sub-linearly with the cluster mass ($M_{SB} \propto M_{cluster}^{8/21}$). As we show in figure 10, for most of the range of ISM densities and scale heights we consider, the mass loading given by equation 33 is between $\eta \sim 0.01 - 10$. Only relatively

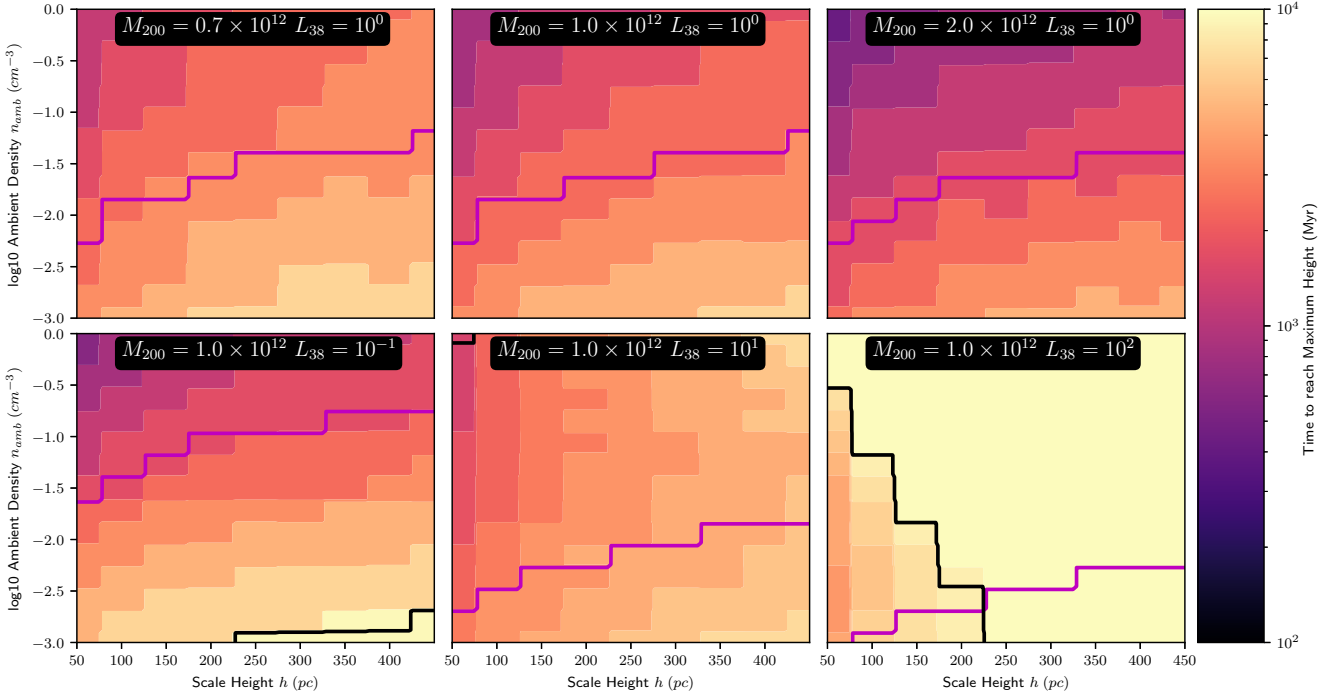


Figure 7. Contour plot of the time required to reach maximum height, for a bubble launched from a number of different ISM conditions, for the same parameters as figure 6. As can be seen here, even for the bubbles which reach the lowest heights, they can rise through the CGM for a \sim Gyr. The purple line shows the time when the bubble will have lost its entropy through radiative cooling (the region above this line cools before it reaches its maximum height). As this shows, the primary determinant of whether a bubble will reach the peak of its buoyant trajectory before cooling is whether or not it is launched from a sufficiently low density ambient medium. The black curve shows where the bubble has not yet reached the maximum height of its flight by the end of our 10 Gyr integration.

low-mass clusters driving bubbles in a dense, thick ISM can produce mass loadings of $\eta \sim 10$. This, however, is the exact same situation which produces bubbles with short cooling times. Only at lower metallicities would these more mass-loaded bubbles be able to spend an appreciable time in the CGM.

This of course assumes that the only material to be ejected at breakout is the hot, well-mixed interior of the superbubble. This is a rather crude approximation, as simulations of superbubbles have shown their breakout to be a turbulent, chaotic process involving multiphase gas spanning orders of magnitude in density and temperature (Joung & Mac Low 2006; Kim & Ostriker 2018; Li et al. 2017; Fielding et al. 2018; El-Badry et al. 2019). Treating this self-consistently is intractable for a simple analytic framework. The results of Kim & Ostriker (2018), for example, show that the mass loadings of warm gas exceeds that of hot gas when measured close to the disc, but that drops precipitously as you move higher, with hot gas mass loadings staying constant at $\eta \sim 0.1$, and that the interactions between the hot and warm/cool phases of the outflow are more complicated than either total entrainment or complete decoupling. We can, however, make some qualitative predictions. First, that the hot, unmixed bubble component provides a floor for the mass loading, as mixed or entrained material will only raise the total amount of material lofted out. This material will increase the mass loading, but also decrease the acceleration of the bubble, reducing the maximum height it reaches. Whether entrained

material will cool the bubble will depend sensitively on the quantity and metallicity of the entrained material, and whether that material stays as cool clouds or mixes efficiently with the bubble. Simulations of cool clouds in fast $v \gg 100 \text{ km s}^{-1}$ winds find that they do mix quickly (Scannapieco & Brüggén 2015), but this can be slowed by the presence of magnetic fields and cosmic rays (Girichidis et al. 2018) or stopped through cloud “shattering” (McCourt et al. 2015; Gronke & Peng Oh 2019). None of these studies, however, have looked at the long-term kinematics and survival of multiphase material in a slowly rising, buoyant outflow. We plan to examine simulations of this scenario in a future study.

Radiative cooling isn’t the only potential instability that may disrupt a bubble as it rises. The bubble itself can be seen as the leading finger of a Rayleigh-Taylor instability, and will thus generate vorticity in its trail, potentially mixing it as it takes the classic “mushroom cloud” shape of a Rayleigh Taylor plume. The edges of the bubble, as well, will experience shear against the background CGM, subjecting them to Kelvin-Helmholtz instabilities. We know from X-ray observations of galaxy clusters that, at least in the extreme AGN-driven case, bubbles can rise to a significant fraction of the cluster virial radius (see for example the $\sim 200 \text{ kpc}$ bubbles observed in MS0735+7421, McNamara et al. 2005) before being completely mixed with the background intercluster medium. Simulations of either AGN-driven (Quilis et al. 2001; Omma et al. 2004; Brüggén et al. 2009; Dong & Stone 2009) or SN-driven (Sarkar et al. 2015) have found that

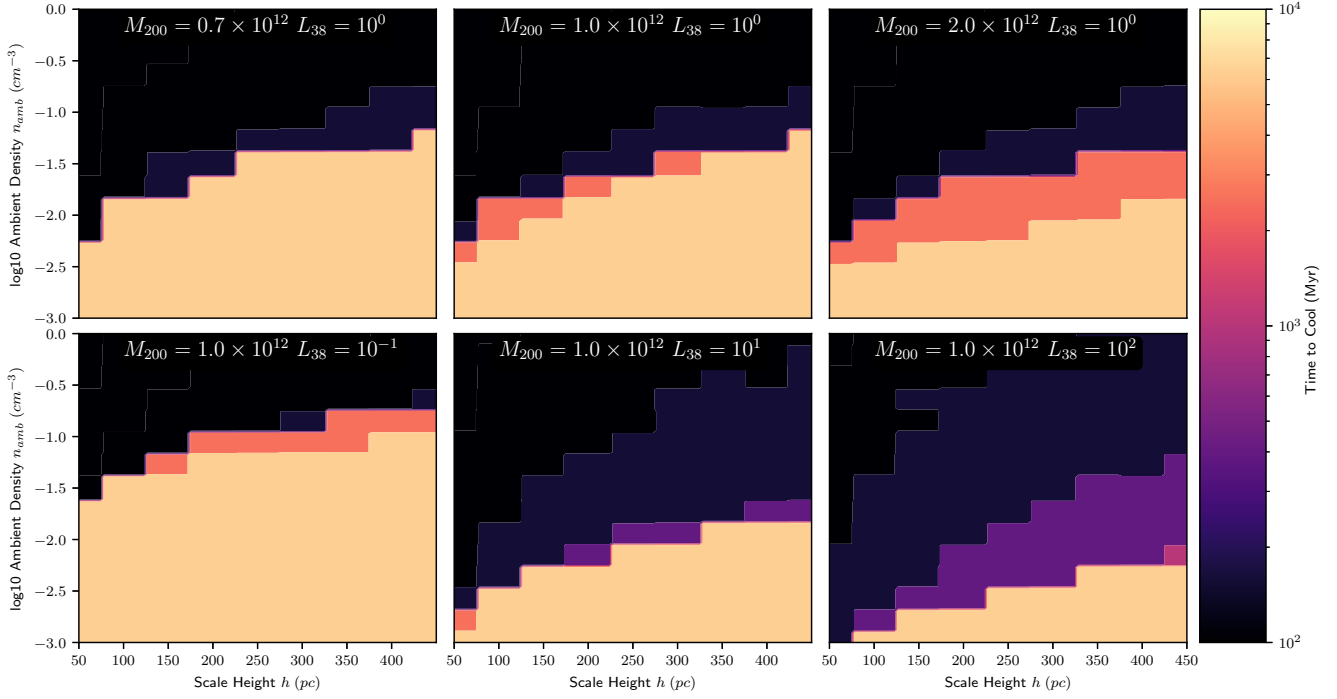


Figure 8. Contour plot of the time when a bubble will radiatively cool, for the same parameters as figure 6. As was seen in figure 7, the density of the ambient medium is the most important factor in determining when the bubble will cool, and for different halo masses/driving luminosities, this density ranges between $\sim 10^{-1} \text{ cm}^{-3}$ and $\sim 10^{-3} \text{ cm}^{-3}$. Paradoxically, bubbles driven by higher luminosity clusters actually require *lower* ambient ISM densities to avoid cooling, because while they result in hotter bubbles, they also result in denser ones at breakout, as $n_{SB} \propto L^{8/21}$.

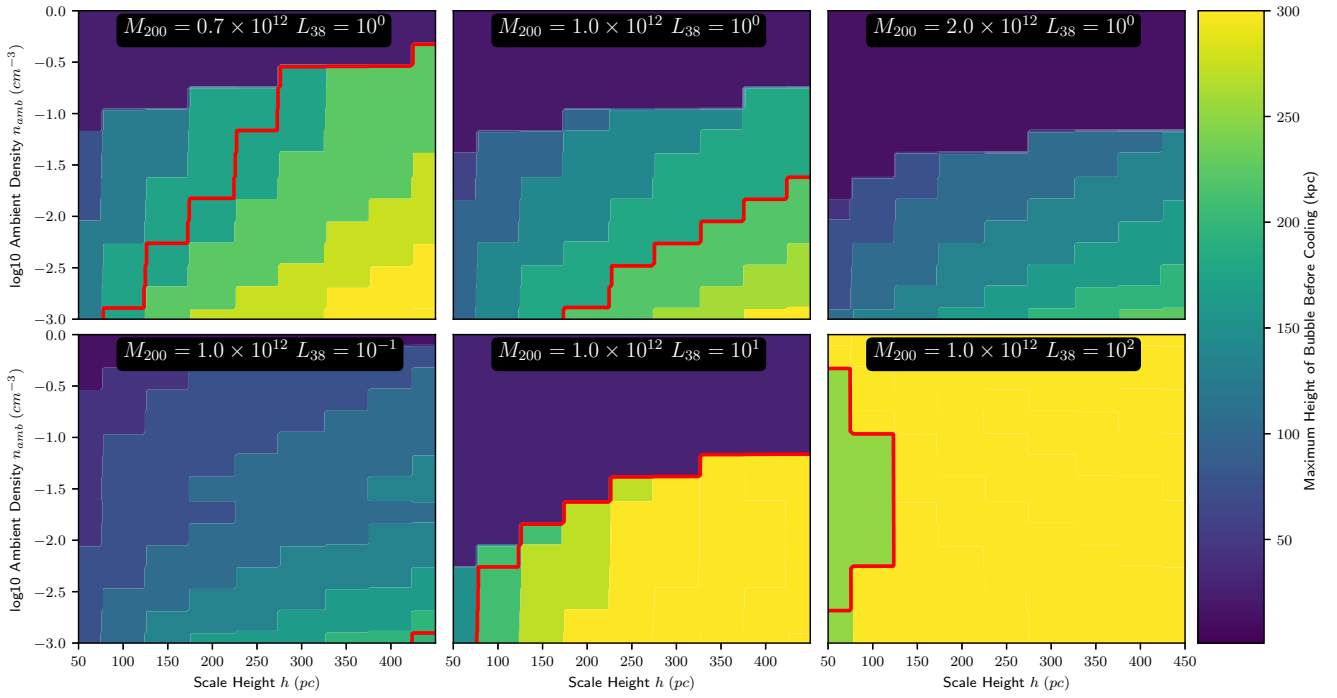


Figure 9. If we assume the bubble's true maximum height is the maximum height it obtains prior to cooling, we can see that, except in the case of our most massive haloes, bubbles are still able to reach appreciable $\sim 100 \text{ kpc}$ heights before they radiatively cool.

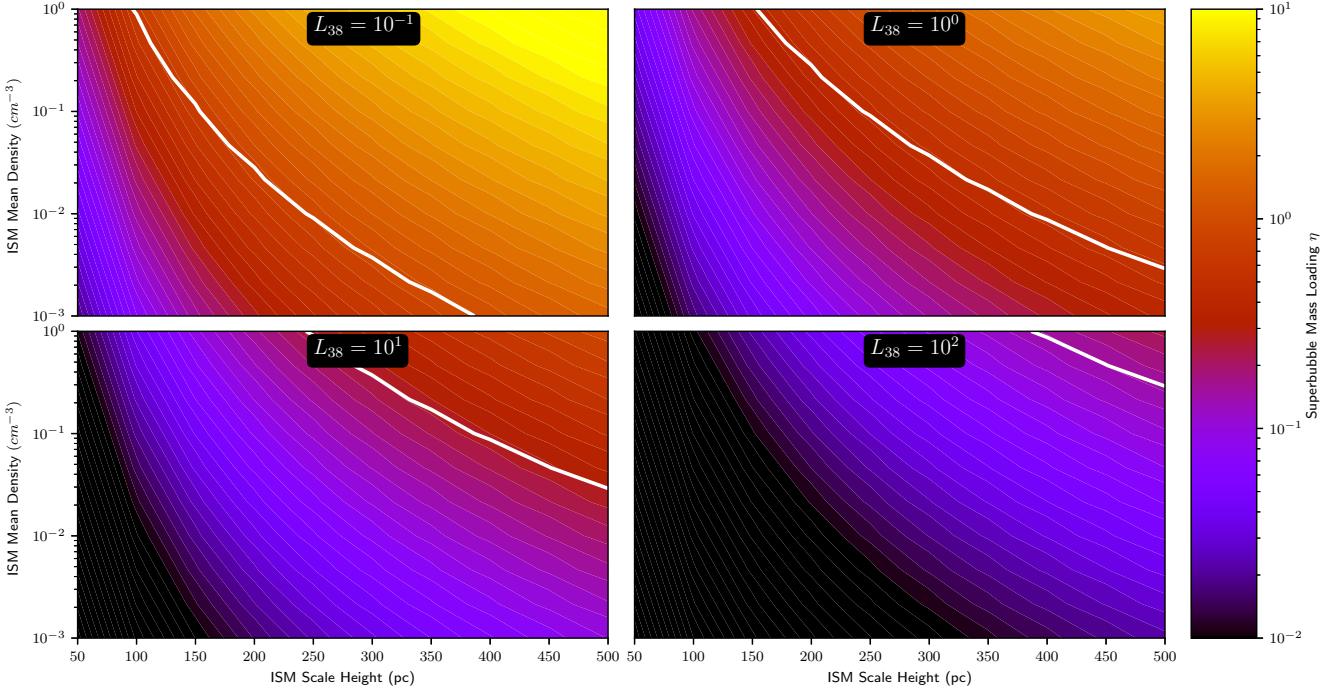


Figure 10. Mass loading ($\eta = M_{SB}/M_{cluster}$) for different mass clusters ($10^3 M_\odot$ in the upper left, $10^4 M_\odot$ in the upper right, $10^5 M_\odot$ in lower left, and $10^6 M_\odot$ in lower right). The white curve shows the region where a bubble will breakout before the cluster shuts off its feedback (as in figure 2). Bubbles driven in regions to the right of this curve will not breakout before the end of SN feedback. As can be seen here, for most clusters in a reasonable ISM, the mass loadings are modest, with $\eta < 1$. Larger mass loadings will be driven only from a dense, thick ISM.

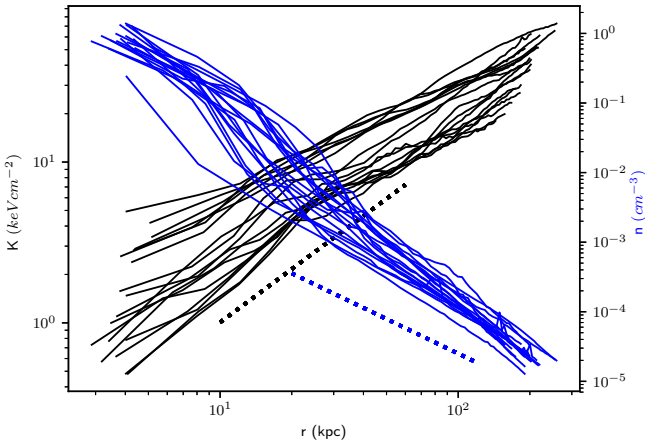


Figure 11. Entropy and density profiles for the 18 MUGS2 galaxies. The left panel shows the volume-averaged entropy for each galaxy in black, while the right panel shows the volume-averaged density profile for each galaxy in blue. The dotted curves show the fiducial $\alpha = 1.1$ slope for the entropy profile, and the corresponding hydrostatic $\beta = 3/2\alpha$ slope for the density profile. While the inner part of the density profile is noticeably steeper than the hydrostatic solution (in large part due to the contribution of the disc), the outer parts of the halo do appear to be in rough hydrostatic equilibrium with a power-law entropy slope of $\alpha = 1.1$.

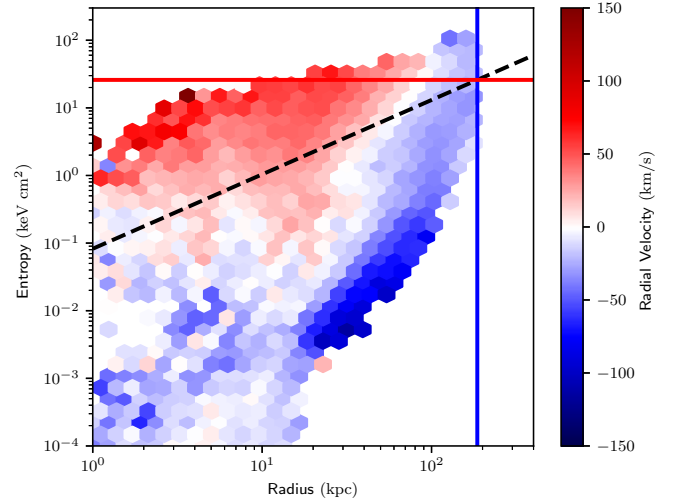


Figure 12. Mean radial velocities as a function of entropy and radius. As in figure 1, we show the virial entropy with the horizontal red line and the virial radius with the vertical blue line. The CGM entropy profile, as given by equation 22, is shown with the black dashed line. As can be seen here, the outflow velocity generally increases as the entropy exceeds the CGM entropy profile, while the inflow velocity increases the further below the entropy profile a parcel resides (and the closer it gets to the bottom of the potential well).

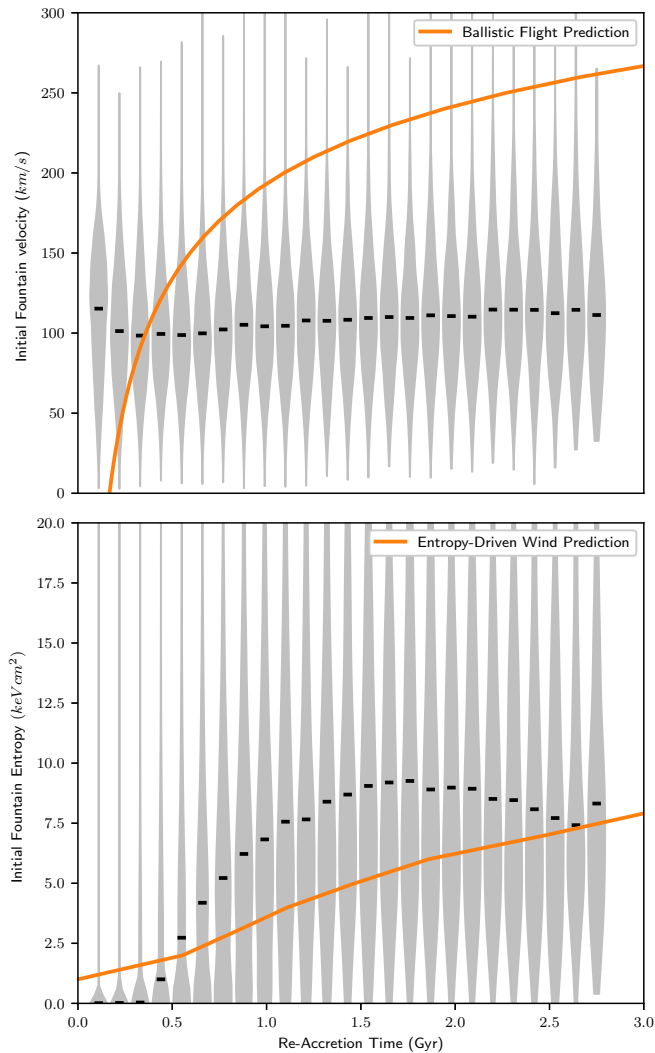


Figure 13. In a simulated L^* galaxy near $z = 0$, outflow re-accretion times for fountain gas have almost no relation to the velocity at ejection, with most fountains having an initial velocity of $\sim 100 \text{ km s}^{-1}$. If we instead look at the typical entropy of ejected gas, we can see that longer-lived $> 2 \text{ Gyr}$ fountains are dominated by gas with higher entropy $\sim 5 - 10 \text{ keV cm}^2$. Median values for the fountain initial velocity and entropy are shown with black lines, and the predictions for the flight of a ballistic and entropy-driven fountain are shown with the orange curves, assuming a gas scale height of 200 pc and a mean ISM density of 1 cm^{-3} , driven by a cluster with a mechanical luminosity of $10^{38} \text{ erg s}^{-1}$.

wind-driven bubbles do experience both classic RT-like instabilities, as well as more complex non-linear turbulent mixing. Interestingly, the simulations of SN-driven starbursts presented in (Sarkar et al. 2015) found that the mixing in the CGM can actually increase the mass loading near the virial radius by up to a factor of 10-40 by sweeping up CGM material. The Kelvin-Helmholtz instability was analytically shown to be suppressed in the presence of viscosity or in inviscid bubbles when there is a significant difference in the mass density of the bubble and the light fluid by (Kaiser et al. 2005). They find that for Rayleigh-Taylor in-

stabilities, only viscous effects producing an effective surface tension can preserve the bubble. Even with a conduction coefficient 100 times below the standard Spitzer value, a magnetic field of a few μG can stabilize the bubble. We would also expect to see much longer Rayleigh-Taylor timescales in the shallower potential well of an L^* galaxy (compared to the $\sim 10^{14} M_\odot$ halo these studies examined), as the growth time scales linearly with the Keplerian velocity. However, as (Dong & Stone 2009) showed, the relatively high magnetic field strengths that do stabilize bubbles in 3D hydrodynamic simulations require specific geometries, and are generally higher than what is observed in the ICM of clusters such as Virgo.

These hydrodynamic instabilities mean that our treatment of the bubble as an arbitrarily long-lived object, subject only to radiative cooling is at best a rough approximation. Long-term oscillations about the buoyant equilibrium radius, as seen in figure 3 will not occur if the bubble is mixed into the CGM. If a bubble were to fragment as it rises, this will naturally increase the overall surface area of the high-entropy gas, increasing the drag forces it would experience. Despite this, there are two reasons we do not expect that bubble fragmentation will completely halt an entropy-driven outflow. First is that the drag forces experienced by a bubble are most significant during the very early evolution of the bubble, when it is accelerated to the highest velocities and it travels through the densest part of the CGM. If the timescale for a bubble to fragment is longer than the time it takes to rise above the dense inner CGM, drag forces become unimportant regardless of surface area at the lower velocities the bubble spends most of its lifetime at. Second, if a bubble fully mixes with the CGM, it may actually stabilize the CGM against radiative cooling, increasing the entropy of region it mixes into if it mixes below the buoyant equilibrium radius or by driving turbulence in the CGM (acting thus as a kind of preventative feedback). Simulations by (Dalla Vecchia et al. 2004; Brüggen et al. 2009; Dong & Stone 2009) all show that while mixing is significant as an AGN-heated bubble rises, it will still reach significant $> 100 \text{ kpc}$ altitudes prior to being fully mixed with the surrounding medium. When a buoyant bubble mixes with the CGM, as long the subsequent material is sufficiently distant from the galaxy disc that it will not rapidly cool and re-accrete, it will still act to transport mass and metals out of the ISM. In certain circumstances, however, the opposite effect may take place, and bubbles driven out of the ISM may actually seed radiative cooling (Marasco et al. 2012) or “precipitation” from the CGM (Voit et al. 2017, 2019), increasing the accretion rate onto the galaxy.

The uncertainty around how multiphase gas arises in galactic outflows (whether it be through entrainment, in-situ cooling, or some other mode) is tempered by both observational and (albeit low-resolution) simulation evidence. In the CGM, hot ($T > 10^6 \text{ K}$), and warm-hot ($T \sim 10^{5.5} \text{ K}$) gas has been observed in a wide variety of environments (Werk et al. 2016; Stocke et al. 2013), but so has cool $T \sim 10^4 \text{ K}$ (Tumlinson et al. 2013), or even molecular gas (Leroy et al. 2015). Meanwhile, simulations of L^* and larger galaxies have found significant mass loadings (Keller et al. 2015; Muratov et al. 2015; Christensen et al. 2016; Mitchell et al. 2019), with much of this mass being carried by cool material. Bridging the gap between high-resolution, small scale simu-

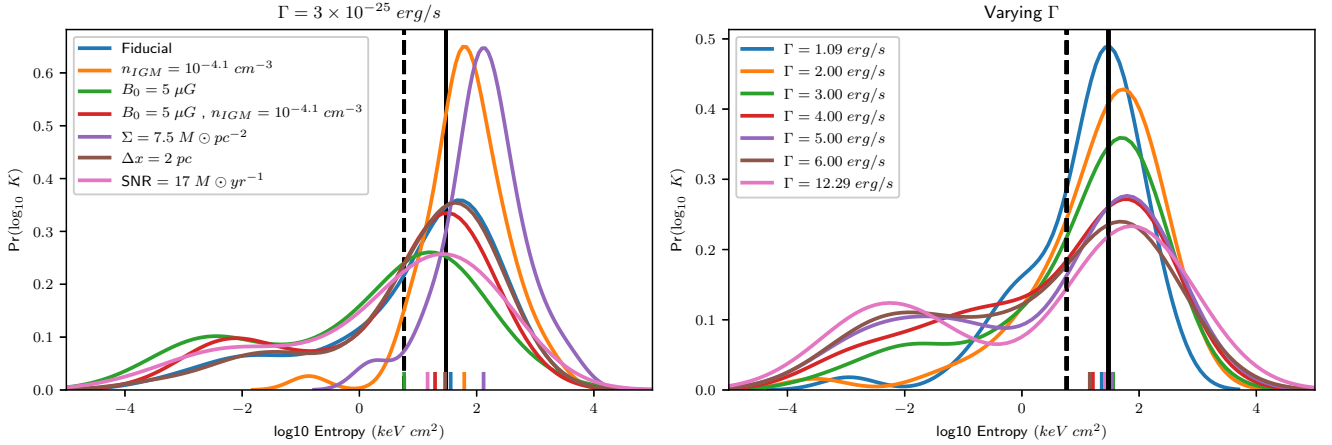


Figure 14. Entropy distribution kernel density estimation of the inner 20 pc of superbubbles in 14 different simulations from Hill et al. (2018b). The left hand panel shows variations in the resolution, supernova rate, ISM and IGM density, and magnetic field properties, while the right hand panel shows the results of varying the intensity of UV heating on the ISM, with the same properties as the fiducial simulations in the left panel. As can be seen, every case produces a significant amount of high-entropy gas, even above the 30 keV cm^2 (shown as the solid black vertical line) required to be neutrally buoyant at the virial radius of a $10^{12} M_{\odot}$ halo, and well above the 5.8 keV cm^2 normalization in equation 15 (shown as the vertical dashed black line). The right hand panel shows that higher heating rates Γ result in a broader distribution of entropies, likely due to a larger fraction of the ISM existing in intermediate densities between the cold and hot phases. As might be expected, both magnetic fields and lower SN rates reduce median entropy produced by superbubbles, while a lower gas surface density or a cooler, denser CGM results in much higher entropy bubbles. The rug plot at the bottom of the x axis shows the median entropy for each simulation. As this shows, there is much greater variation in the median entropy in the left hand panel.

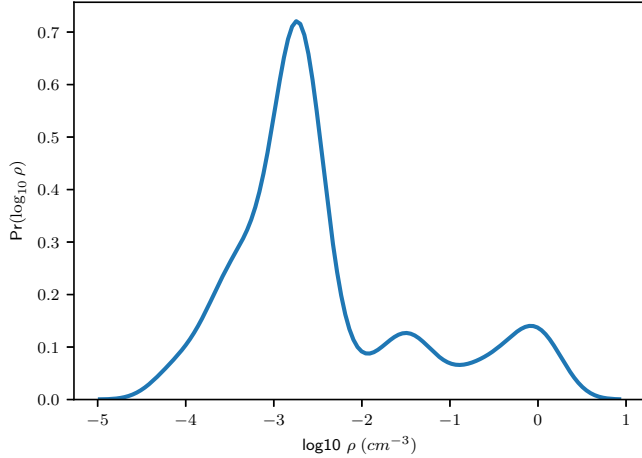


Figure 15. Density distribution of the 20 pc sphere surrounding each pre-supernovae star particle in the Hill et al. (2018b) simulations. As is clear here, the majority of SN detonate in a region with significantly lower density than 1 cm^{-3} , with most occurring in regions with densities $\sim 10^{-3} \text{ cm}^{-3}$. This is due to a combination of stellar winds pre-treating the ISM, heating and disrupting dense gas; and the random positioning of star clusters, so that many detonate in the low density, hot superbubbles of older star clusters.

lations and the observational/simulation evidence on larger scales that suggest a ubiquitous, multiphase ISM will require serious work both on the analytic, theoretical front as well as in more sophisticated numerical modelling.

4 COMPARISON TO SIMULATIONS

4.1 Cosmological Simulations

If cosmological simulations are run with adequate resolution (Muratov et al. 2015) and sub-grid feedback models (Keller et al. 2014, 2015) to generate ab-initio winds of hot, high-entropy gas, we should expect to see outflows being driven by entropy gradients, with the long recycling times and relatively low velocities that entropy-driven wind theory predicts.

Here we compare to simulations from the McMaster Unbiased Galaxy Simulations 2 (MUGS2) sample of galaxies. MUGS2 is a set of 18 cosmological zoom-in simulations, focusing on the evolution of L^* galaxies with a range of merger histories and spin parameters, selected without biasing to reproduce any given single object. These galaxies were simulated in a WMAP3 ΛCDM cosmology, with parameters $H_0 = 73 \text{ km s}^{-1} \text{ Mpc}^{-1}$, $\Omega_M = 0.24$, $\Omega_{bar} = 0.04$, $\Omega_{\Lambda} = 0.76$, and $\sigma_8 = 0.76$. The MUGS2 $z = 0$ halo masses range from $3.7 \times 10^{11} M_{\odot}$ to $2.2 \times 10^{12} M_{\odot}$, with disc masses ranging from $1.8 \times 10^{10} M_{\odot}$ to $2.7 \times 10^{11} M_{\odot}$. The details of how the initial conditions for these galaxies were built can be found in the first MUGS paper, Stinson et al. (2010).

Each of these simulations has a gas mass resolution of $M_{\text{gas}} = 2.2 \times 10^5 M_{\odot}$, and uses a gravitational softening length of $\epsilon = 312.5 \text{ pc}$, and a minimum SPH smoothing length set to 1/4 of this. We use a simple Schmidt-law star formation prescription (Katz 1992), with an efficiency per freefall time of 0.05. Star formation can occur in gas that with density exceeds $\sim 10 \text{ cm}^{-3}$, and temperature below $1.5 \times 10^4 \text{ K}$. A critical difference between the MUGS and MUGS2 simulations is the introduction of the Keller et al. (2014) superbubble feedback model. This model

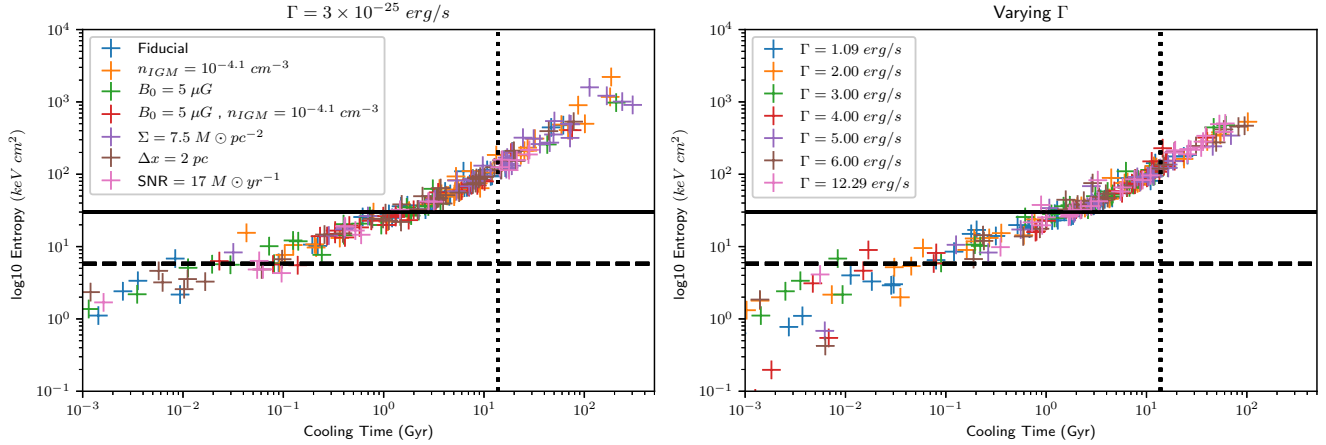


Figure 16. Cooling times versus entropies for each superbubble in the Hill et al. (2018b) simulations. The vertical dotted line shows a Hubble time, and the two horizontal lines show the virial entropy of $10^{12} M_{\odot}$ halos 30 keV cm^2 (solid line) and the typical bubble entropy at breakout, 5.8 keV cm^2 (dashed line) respectively. As is clear, essentially every superbubble with an entropy above 5.8 keV cm^2 has a cooling time longer than 100 Myr, and the majority of superbubbles have cooling times exceeding 1 Gyr, as would be expected from figure 5 and figure 15. Superbubbles with short cooling times would already not be able to rise buoyantly (due to their low entropy) even if they could break out of the ISM before cooling.

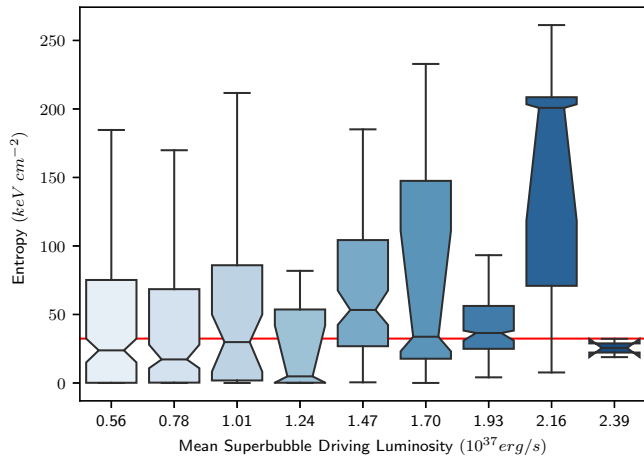


Figure 17. Box plot of the entropy distribution of superbubbles binned as a function of the SN luminosity of their star clusters. The red horizontal line shows the median entropy of 32 keV cm^2 . The box heights are the interquartile range, while the whiskers show 1.5 times the IQR. The notches show the bootstrapped 95% confidence interval for the median values in each bin. No clear trend with luminosity is obvious for this range of cluster masses.

captures the effects of thermal evaporation, as described in (Cowie & McKee 1977; Weaver et al. 1977) in order to determine the proper amount of hot gas heated by SN feedback (Mac Low & McCray 1988). This allows the superbubble feedback model to generate high entropy, buoyant gas, as was described in Keller et al. (2015, 2016).

In figure 11, we show the entropy and density profiles for each of the MUGS2 galaxies. As can be seen, each can be roughly described as a power law, with slopes consistent with an entropy profile with $\alpha = 1.1$. The break in the density slope around 10 kpc is due to the edge of the thick disc ISM contributing mass to the profile. It can be seen here as well

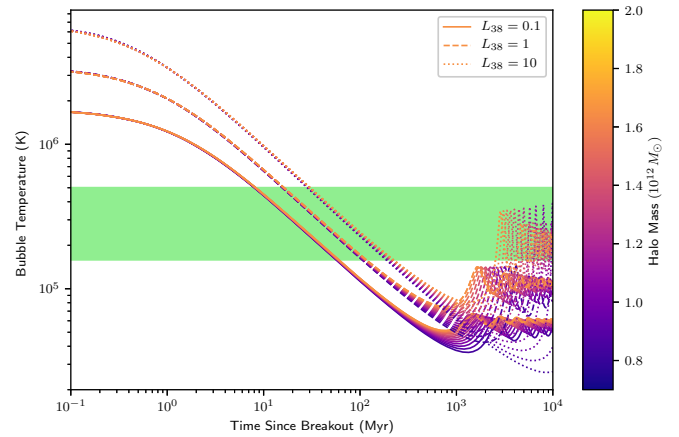


Figure 18. Temperature of the bubble as it rises through the CGM. The green band shows the region where the OVI ionization fraction exceeds $f_{\text{OVI}} = 0.02$ (Tumlinson et al. 2011). While the bubble spends most of its lifespan below the critical temperature $T^{5.2-5.7} \text{ K}$ where OVI is abundant, it does spend a few 10 – 100 Myr during its flight in this temperature range, where it in principle should be detectable in absorption by COS and other UV instruments. For bubbles driven by more massive clusters, the oscillations about buoyant equilibrium may also push the bubble temperature back towards this temperature as it heats and cools through PdV work.

that the normalization of the entropy profile increases with mass (the highest entropy profile corresponds to the galaxy with $M_{200} = 2.2 \times 10^{12} M_{\odot}$, which has a virial entropy of $\sim 60 \text{ keV cm}^{-2}$ as per equation 6).

If we take a look at the MUGS2 “fiducial” galaxy, g1536, we can see that the entropy profile can be broken into two components (as was seen in figure 1): a cooling, inflowing component, and hot, outflowing component. In figure 12, we take this data and bin by radius and entropy, weighting each

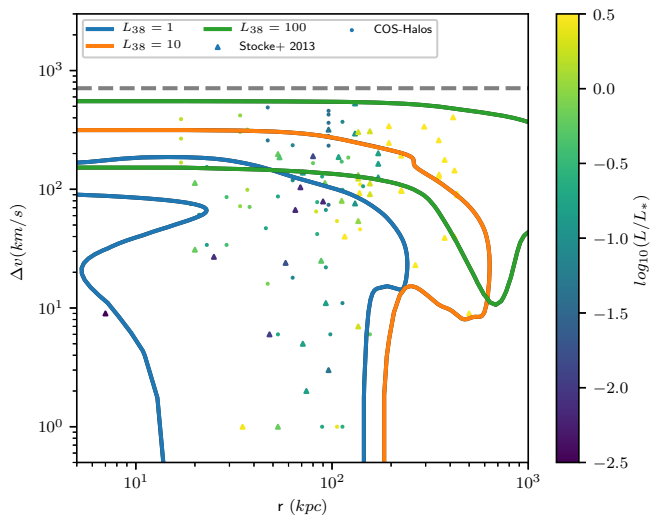


Figure 19. Here we show a comparison between the velocities and positions of entropy-driven wind bubbles and observations from the HST-COS instrument. We show contours outlining the regions in phase space where the bubble finds itself for 3 different driving luminosities in a $7 \times 10^{11} M_{\odot}$ halo. As can be seen here, a range of cluster masses can explain all of the structure we see, and in fact, different ranges of this phase space may point to driving by different luminosity sources. Data points are from [Stocke et al. \(2013\)](#) and [Tumlinson et al. \(2013\)](#), shown with triangles and dots respectively, coloured by their host galaxy luminosity. The grey dashed line shows the escape velocity for a halo with virial mass $7 \times 10^{11} M_{\odot}$, $\sim 700 \text{ km s}^{-1}$.

bin by the mean velocity of gas in the bin. As can be seen in this figure, we do indeed see higher outflowing velocities in gas with entropy above the profile given by equations 6 and 22. Gas below this curve is almost exclusively inflowing, except for a small amount of material at $r \sim 20 - 50 \text{ kpc}$. This material may either be entrained gas, swept up by drag on passing superbubbles, or it may actually be a signature of the convective overshoot seen in figure 3. However, if we consider the mass bins shown in figure 1, we can see that this overshoot/entrained material actually accounts for very little mass.

The key difference between entropy-driven and ballistic fountains is the relationship between the outflow velocity and the distance it can travel from the galaxy before re-accreting, as well as the time it takes to do so. By looking at the final 3 Gyr of evolution for our simulated galaxy, we can examine fountain re-accretion unimpeded by either significant merger activity (which can easily be mistaken as outflowing/fountain material as it recedes from its pericentric pass) and also compare to the evolution predicted by equation 32, with a fairly constant virial mass (the $z = 0$ virial mass of g1536 is $\sim 7 \times 10^{12} M_{\odot}$). By selecting gas particles that cross a spherical surface around the center of the halo, with radius $0.1R_{200}$, we can select fountain particles (those going from inside to out) and re-accreting particles (those going from outside to in). Tying fountain particles to their re-accretion allows us to track the total time spent in the fountain and compare this to the state of the gas as it is ejected. In figure 13, we show the velocity and

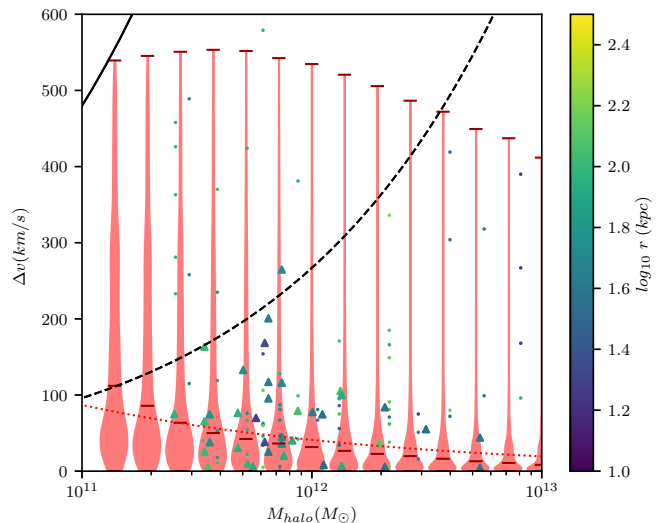


Figure 20. Outflow velocity as a function of halo mass. Data points are from COS-Halos, either the full data set (shown as small circles) ([Tumlinson et al. 2013](#)), or from the subsample of highly ionized sources from ([Werk et al. 2016](#)) (large triangles). Predictions for the velocity of entropy-driven winds from a range of ISM densities ($10^{-3} - 1 \text{ cm}^{-3}$) and scale heights ($50 - 500 \text{ pc}$) for different halo masses are shown as violin plots. The horizontal lines in the violin plot show the most extreme data points (top) and median values (bottom). The dotted red curve shows a power-law fit to the highly ionized COS-Halos sources. The solid and dashed black curves show the escape and virial velocities respectively.

entropy of gas particles identified in fountains as a function of the fountain events re-accretion time. We bin each fountain event based on the re-accretion time, which allows us to look at the distribution of ejection velocities (top panel) and entropies (bottom panel) for fountain events that are re-accreted over a range of timescales. As this figure shows, there is very little relationship between the velocity and re-accretion time, with most fountain events having initial velocities of $\sim 100 \text{ km s}^{-1}$, and none having initial velocities above 350 km s^{-1} . We show the predicted fountain recycling time here for different initial velocities in a halo with the same mass as g1536. Comparing the simulation results to this prediction, we can see that the fountain events which re-accrete in $> 500 \text{ Myr}$ are travelling far too slowly to be simply evolving ballistically. If we instead look at the entropy of fountain flows at their launching, we can see that higher entropy outflows persist for longer prior to re-accretion, with low entropy gas ($K < 2 \text{ keV cm}^2$) returning in $\sim 500 \text{ Myr}$. High-entropy gas ($K > 5 \text{ keV cm}^2$), with entropies typical of what we expect for SN-driven superbubbles (given by equation 15) on the other hand re-accretes on longer timescales, $> \text{Gyr}$, comparable to the predicted evolution for a bubble of different initial entropies travelling through the same halo as is used for the ballistic lifetime predictions.

An important feature to note in figure 13 is the direction of the offset between the median velocity/entropy and the predicted velocity/entropy for the range of fountain lifetimes shown. The ballistic predictions for the fountain velocity are a lower limit for the lifetime. In these calculations,

we have omitted the drag term used in equation 32 to allow the largest possible recycling times given the uncertainty of ballistically-driven winds interacting with the CGM. Any drag or mixing will act to decelerate the outflow, pushing the orange curve further towards the upper left of the plot, and increasing the difference between the simulation results and the ballistic theory prediction. On the other hand, our calculations for the flight of entropy driven outflows have included the effects of drag, but omitted the effects of cooling. Mixing, stronger drag, or radiative cooling will sap the bubble of momentum or entropy, causing it to re-accrete sooner. This also will move our prediction up and to the left, bringing it into better agreement with the simulation data. A full 3D simulation treatment including hydrodynamic mixing and radiative cooling is left for future work.

4.2 Superbubble Entropy Generation in a Realistic ISM

The derivations presented thus far make a number of simplifying assumptions about the growth of a superbubble within the ISM, prior to its break out and buoyant uplift through the CGM. We can test our simple, one-dimensional model by comparing it to data from simulations of a more realistic, self-consistent interstellar medium. Recent studies have been able to investigate the break out of galactic winds from tall, stratified slices of the ISM, achieving resolutions of \lesssim pc. Not only do these simulations offer significantly better resolution, down to the ability to resolve the effects of individual massive stars, they also have included physics that is often omitted from larger cosmological simulations, such as magnetic fields, cosmic rays, and radiation hydrodynamics. We can use the publically available data from these simulations to verify our assumptions about the entropy of the hot interior of the superbubble, prior to break out. We use here the simulations of Hill et al. (2018b). These simulations are run with a wide variety of different physical processes, all using the FLASH code (Fryxell et al. 2000).¹

Hill et al. (2018b) presents a suite of 22 simulations of a $1 \times 1 \times 40$ kpc xy-periodic slab of the ISM with outflow boundary conditions in the z-direction. These simulations have varied gas surface densities, gas densities above the disc, magnetization, resolution, and (the primary change) ISM heating rates. Each of the simulations includes radiative cooling (Joung & Mac Low 2006) (assuming solar metallicity) and a heating rate designed to approximate photoelectric heating of dust grains. This heating rate has an exponential falloff with height above the midplane, with a scale height of 8.5 kpc. The initial conditions use a fixed gravitational potential, with an initially isothermal disc in hydrostatic equilibrium. The feedback model used in these simulations includes energy injection by stellar winds, type Ia SN, and type II SN. Star particles are created to give a fixed total SFR surface density, with randomly chosen xy positions and an exponential distribution in height, with a scale height of

90pc. During the first 5Myr of a star particle’s lifespan, stellar winds with a luminosity of 10^{36} erg s⁻¹ per massive star are injected, followed by either a single SN (meant to capture the effect of a field core-collapse SN, occurring in 32% of all stars), or between 7 and 40 SN (meant to capture the effect of clustered star formation, occurring in 47% of all star particles). The remaining SN are type Ia SN, distributed with a scale height of 300 pc. Each supernovae deposits 10^{51} erg worth of energy.

The “fiducial” simulations in Hill et al. (2018b) each have a SN rate of $34 \text{ Myr}^{-1} \text{ kpc}^{-2}$, an ISM gas surface density of $13 M_{\odot} \text{ kpc}^{-2}$, and a maximum refinement level of $\Delta x = 4$ pc. A range of different photoelectric heating rates, from $1 \times 10^{-25} \text{ erg s}^{-1}$ to $1.23 \times 10^{-24} \text{ erg s}^{-1}$. Two runs are done using a horizontal magnetic field of $5 \mu G$ at the midplane, which decreases with height to maintain constant magnetic β . Two runs are done with a reduced gas surface density of $7.5 M_{\odot} \text{ kpc}^{-2}$, and two are done with a hotter, more diffuse IGM/CGM (one with and one without magnetization). Resolution is also varied, with $\Delta x = 2$ pc and $\Delta z = 1$ pc. The final additional run is a test with a reduced SN rate of $17 \text{ Myr}^{-1} \text{ kpc}^{-2}$. We have selected a subsample of these simulations to see if the entropy generation in a fully 3D, turbulent ISM that includes radiative cooling, magnetic fields, and the pre-heating of SN regions by stellar winds can generate hot gas with similar entropies to what is predicted by equation 15.

The publically available data provided from Hill et al. (2018b) includes a record of where each massive star cluster is placed, as well as when it was formed and how many SN have detonated. We select each star that particle that has formed between $t = 160$ Myr and the final timestep of $t = 200$ Myr, and select (mass-weighted) gas within a 20 pc sphere around these particles in this final output. This allows us to examine regions where SN have detonated, but have not yet had a chance to vent out of the ISM. We also select a smaller subsample of star particles that have formed between $t = 195$ Myr and $t = 200$ Myr to examine the density of the ambient ISM which SN are detonated in. Naturally, these small, young superbubbles may not have the same entropy at breakout as they do when they may break out of the ISM. Subsequent mixing of cool gas or radiative cooling may act to reduce the entropy of this material before it breaks out. Therefore, the values measured here should be seen as upper limits to the entropy at breakout. Tracking material through the halo is also, unfortunately, impossible to do with simulations at such high resolution. The resolution that allows us to treat the ISM’s multiphase structure in detail also limits us to studying only small slices of the disc in a stratified, periodic box.

We use these data to examine three predictions made by our simple 1-dimensional calculations: that sufficient entropy is generated inside superbubbles by SN to make the superbubbles strongly buoyant, that these superbubbles have sufficiently long cooling times to actually escape the ISM and expand adiabatically, and that the superbubble’s entropy is only weakly dependent on the star cluster’s driving luminosity. As can be seen in the entropy Kernel Density Estimate (KDE), figure 14, regardless of the wide variety of parameters and physics included in the different Hill et al. (2018b) simulations, we find the majority of superbubbles produce gas with an entropy $> 10 \text{ keV cm}^2$, with a small

¹ The simulation outputs from Hill et al. (2018b) are all publically available, and are accessible at the American Museum of Natural History Research Library Digital Repository Hill et al. (2018a)

number superbubbles “failing”, due to their detonation in particularly dense environments with short cooling times. In every case, the median entropy of superbubbles in the simulation is above the normalization in equation 15. The magnetized case appears to produce the lowest entropy superbubbles, while the case with lower gas surface density produces the highest median entropy. The variation in the median entropy induced by varying the photoelectric heating rate is fairly small: it appears that a higher heating rate produces a broader distribution of superbubble entropies, but little change in the median value of this distribution.

If we look specifically at the environment around stars which have not yet detonated any SN, we can see in figure 15 that the majority of SN detonate within gas with an ambient density of $\sim 10^{-3} \text{ cm}^{-3}$. This is important both to increase the entropy of the superbubble, and to reduce the cooling time. As we see in figure 16, essentially all superbubbles with $K_{SB} > 10 \text{ keV cm}^2$ have cooling times $> 100 \text{ Myr}$, and those which would be positively buoyant all the way to a virial radius in a $10^{12} M_{\odot}$ halo have cooling times $> \text{Gyr}$. These cooling times will increase as well, as the bubble rises through the CGM and becomes more diffuse (as we saw in figure 5). The range of SN detonated by each star particle in the Hill et al. (2018b) simulations also lets us probe the dependence of superbubble entropy on the SN luminosity of the star cluster. A cluster with N_{SN} detonated over a period of 40 Myr will have a luminosity $L_{SB} = 7.93 \times 10^{35} N_{SN} \text{ erg/s}$. We can bin all of the star particles in the Hill et al. (2018b) by the number of SN detonated to see, as we show in figure 17, to examine whether there is any significant trend in the entropy generated versus the cluster luminosity. As we can see, there is a fairly large scatter in the superbubble entropy, owing to the inhomogeneous ISM and the different ages of the superbubbles. The median entropy of the full sample of superbubbles is 32 keV cm^2 , and as is clear, there isn’t an obvious trend with increasing cluster luminosity. In the range of luminosities we see here, assuming identical ambient ISM conditions, we should only see an entropy increase of 5% between the smallest ($N_{SN} = 7$) and largest ($N_{SN} = 40$) clusters. This is much smaller than the scatter we see here, and thus it is unsurprising that no trend is noticeable. The small IQR seen in the final bin is simply a function of a small number of clusters actually falling within that bin. It is important to note, though, that the Hill et al. (2018b) simulations do not use a self-consistent star formation recipe, but instead randomly place star clusters within 90 pc of the disc mid plane. This will certainly somewhat over-estimate the number of SNe detonating in low-density environments. Future studies looking at the driving of superbubbles, with self-consistent ISM and disc structure will be able to quantify this in much greater detail.

5 COMPARISON TO OBSERVATIONS

The HST COS instrument (Green et al. 2012) has produced a number of unprecedented surveys of the CGM of L_* galaxies. By probing absorption of background QSO spectra by the resonant OVI doublet at $T \sim 10^{5.2-5.7} \text{ K}$ (Tumlinson et al. 2011), it is able to detect out-of-equilibrium warm-hot gas without relying on either high column densities needed to see neutral/molecular clouds, or

the higher temperatures needed to detect CGM gas through X-ray emissions. In the last 5 years, a number of large $N > 10$ surveys of absorption systems surrounding $\sim L_*$ galaxies have been produced that constrain the mass, structure, and kinematics of these galaxies’ CGM (Stocke et al. 2013; Tumlinson et al. 2013; Werk et al. 2014, 2016). These studies probe samples of galaxies at different impact factors (angular separation between the galaxy and QSO, a lower limit on the radial distance between the galaxy and the absorber) at fairly low redshift $z \sim 0.2$. Werk et al. (2016) presented an interesting reduction of the COS-Halos data, selecting in particular galaxies with active star formation, relative isolation, and positive detection of OVI within their inner CGM. These are a “cleaner” subsample of the full COS-Halos dataset as they are least likely to be contaminated by material stripped from interacting haloes.

In figure 18, we show the temperature evolution of a bubble as it rises through the CGM, while remaining in pressure equilibrium with the surrounding medium. As it rises and expands, the bubble’s initial temperature decreases adiabatically. Naturally, bubbles driven by larger clusters have higher initial temperatures at breakout, but significantly less than the 2 orders-of-magnitude difference in mechanical luminosity. As can be seen in the green band, the bubbles pass through the temperature range where OVI absorption would be strong ($f_{OVI} > 0.02$) for a few 10–100 Myr, and for bubbles driven by larger clusters, will be detectable in the CGM as they oscillate back down to higher CGM pressures, when their temperatures increase from adiabatic compression. While this timeframe is a relatively small fraction of the time the bubble spends in the CGM, a star forming disc, producing multiple star clusters continuously driving feedback, will populate the the CGM with multiple bubbles at different heights, giving a detectable signature throughout the halo. It is also possible that bubble material may mix with hotter material in the CGM, cooling it to the temperatures where OVI will be detectable. During the bubble’s initial flight, when it’s temperature is above the narrow range where OVI abundance is high, entrained cool material from the ISM would also produce OVI absorption features in the mixing layer between these cooler clumps and the hot bubble material.

Here we compare our predicted radius-velocity phase-space behaviour to the observed data from two of these studies, Stocke et al. (2013) and Tumlinson et al. (2013). Both of these focused on galaxies near L_* , and probed the kinematics of CGM absorbers out to a few R_{200} . As we see in figure 19, none of the observed CGM absorbers found in these COS observations exceed the escape velocity of a $\sim L_*$ galaxy, with $M_{halo} = 7 \times 10^{12} M_{\odot}$ and $v_{esc} \sim 700 \text{ km s}^{-1}$. There also appears to be little relation between the impact factor of the observation and the velocity centroid, with velocities of a few to a few 100 km s^{-1} seen from $\sim 10 \text{ kpc}$ out to $\sim 300 \text{ kpc}$, beyond the virial radius of most of these galaxies. We show contours of the predicted phase-space behaviour for entropy driven outflows for a $7 \times 10^{11} M_{\odot}$ halo being driven by clusters with luminosity (mass) of $10^{38} \text{ erg s}^{-1}$, $10^{39} \text{ erg s}^{-1}$, $10^{40} \text{ erg s}^{-1}$ ($10^4 M_{\odot}$, $10^5 M_{\odot}$, $10^6 M_{\odot}$). As these contours show, entropy-driven outflows can produce outflowing material at the same radii, with the same velocities as the warm OVI absorbers observed by COS.

COS-Halos selected galaxies in part based on their

SDSS k -corrected masses derived from *ugriz* magnitudes, giving a dataset which includes estimates of the total stellar mass and SFR for their sample of galaxies. Using these stellar masses, we can use a stellar mass to halo mass relation (SMHMR) determined either through abundance matching (Behroozi et al. 2013) or directly with weak lensing (Hudson et al. 2015). Here, we use equation C1 from the CFHTLenS observed SMHMR to determine halo masses for each of the galaxies in COS-Halos, to compare with the predictions of entropy driven winds in different mass haloes. As we see in figure 20, outflowing metals are seen with a wide range of velocities, without a strong dependence on halo mass. We show the predicted range of velocities as time-weighted violin plots (as the longer gas stays at a given velocity, the higher its chance of being observed at that velocity) for a range of different halo masses, using the same range of ISM densities and scale heights as figures 6, 7, and 19. As can be seen from these violin plots, entropy-driven winds can produce some high-velocity outflows (in the cases of very high-luminosity clusters driving outflows from a very low density, thick ISM) even up to $M_{200} = 10^{13} M_{\odot}$, but both the median and maximum velocities decrease at higher halo mass. A fit to the Werk et al. (2016) subsample finds that the typical outflow velocity is $v_{out} \sim 30(M_{halo}/10^{12} M_{\odot})^{-1/3} \text{ km s}^{-1}$, in good agreement with the relationship between the median outflow velocity and halo mass for entropy-driven winds from a wide variety of ISM environments. It is also clear that both the observed CGM absorbers from Werk et al. (2016) and the majority of entropy-driven outflows have velocities well below the virial velocity of their parent halo, meaning this gas is bound to the galaxy halo.

6 DISCUSSION

We have examined here the behaviour of a new kind of galactic outflow, driven not by feedback momentum injection in the ISM, but instead through a steady, continuous acceleration through the CGM. This acceleration is a consequence of buoyant force between hot, high entropy gas and the entropy-stratified CGM. The kinematics of entropy-driven winds are able to broadly reproduce both observations of gas flows in the CGM as well as the behaviour of galactic outflows in cosmological simulations of L^* galaxies.

6.1 Ballistic vs. Buoyant Winds

What we have shown through this paper is that the phenomenology of galactic outflows depends heavily on whether one considers the CGM environment through which they travel. Estimates of outflow recycling times, the mass loading of outflows, and the distance which these outflows might reach can be off by an order of magnitude or more if made assuming simple ballistic flight. Simply focusing on the energy budget available from feedback processes or the initial velocity of feedback-heated gas heavily underestimates the effectiveness of outflows at removing significant amounts of gas from the ISM for long, cosmological timescales.

Taking buoyancy into account, and modelling outflows as entropy-driven, rather than simply ballistic, solves a number of issues in galaxy evolution. Outflows which remove

a significant fraction of material from the ISM, can solve both issues with the baryon (Papastergis et al. 2012), stellar (Behroozi et al. 2013), and metal (Peeples et al. 2014) content observed in galaxies. Ballistic outflows recycle on a very short timescale, with $t_{rec} \sim 100 \text{ Myr}$ for L^* galaxies with halo masses $\sim 10^{12} M_{\odot}$. This means that ballistic winds would need to remove material from the ISM 10–100 times to prevent it from forming stars, compared to the 1–10 times required by entropy-driven winds. On top of this, these fountains can rarely exceed apocentric distances of a few 10 kpc, rendering it hard to see how they are able to populate the CGM with metals and cool material out to the $\sim R_{200}$ distances they have been observed (Stocke et al. 2013). Slow-moving winds, with $v \sim 100 \text{ km s}^{-1}$ out to $r \sim 100 \text{ kpc}$ are a natural consequence of allowing outflowing gas to be accelerated through the CGM.

6.2 Comparison with Other Models

The idea of buoyancy as critical feature of SN-driven outflows in L^* galaxies was first explored by Bower et al. (2017). Bower et al. (2017) argues that the transition in galaxy properties seen at $M_{200} \sim 10^{12} M_{\odot}$ is a result of the halo’s virial entropy exceeding the characteristic entropy of supernovae-heated gas. This is similar to what we have explored here, with a few critical differences. Bower et al. (2017) is not a full exploration of the kinematics of entropy-driven outflows, but instead uses a number of simple scaling relations, to derive a characteristic entropy for supernovae-heated gas, with a different functional form to what we have derived here. Unlike our derivations, which follow the evolution of a wind-swept bubble powered by a single star cluster, the Bower et al. (2017) simply parameterize the mass-loading and assume that the ISM density and halo mass follow a simple scaling relation, with $K_{outflow} \propto \eta^{-1}$. While their derivations produce slightly different halo entropy to what we have used here, it is roughly comparable to what we derive in equation 11. Bower et al. (2017) uses their parameterized feedback entropy to suggest that the outflow mass loading η can only be large when it allows $K_{outflow} > K_{halo}$, which limits this to haloes with $M_{200} < 10^{12}$. What we have derived here is a self-consistent model of how the ISM structure and the star formation process sets the entropy of outflowing gas (for most reasonable values of n_{amb} , L_{38} , and h , we find entropies within a factor of a few compared to what Bower et al. 2017 finds), and how this gas actually moves through the CGM. Our results are in broad agreement with the central result of Bower et al. (2017), namely that above $M_{200} = 10^{12} M_{\odot}$ supernovae-driven outflows fail to effectively remove material far beyond the disc of galaxies in $M_{200} \sim 10^{12} M_{\odot}$ haloes (as is shown in figure 9 and 20). However, the simplified assumption that effective outflows require $K_{outflow} > K_{halo}$ ignores two of the key results we have presented here. First, that the CGM’s entropy stratification can allow entropy-driven winds to reach a significant fraction of R_{200} without actually leaving the halo. Second, outflows with entropy below the virial entropy will overshoot their equilibrium radius due to simple momentum conservation, and can take a significant amount of time to either reach their maximum height or to cool and re-accrete.

A recent study (Lochhaas et al. 2018) has produced similar results to what we have shown here, using a quite

different analytic framework. Like this work, [Lochhaas et al. \(2018\)](#) builds on the classic wind-driven shell solutions derived by [Castor et al. \(1975\)](#); [Weaver et al. \(1977\)](#) to predict the kinematics of gas flows within the CGM. Unlike this work, however, [Lochhaas et al. \(2018\)](#) builds off an assumption that the galaxy can be treated as a single luminosity source, with superbubbles escaping from the ISM and combining to form a uniform, spherically symmetric wind-swept bubble. As this shell propagates outward, it sweeps up material from the CGM to build up a fairly slow-moving, massive shell. Despite having a relatively low velocity the wind-swept shell can take $> \text{Gyr}$ to re-accrete, both because the initial wind velocity is high ($\sim 400 - 900 \text{ km s}^{-1}$) and the shell itself is continuously receiving momentum from the wind behind it. [Lochhaas et al. \(2018\)](#) shows that for the majority of the time it spends in the CGM, it travels with modest $\sim 100 \text{ km s}^{-1}$ velocities, and that these kinematics and the column density profile of the shells are consistent with the COS-Halos observations of [Werk et al. \(2014\)](#). Our work differs from this analysis primarily in that we begin with a local treatment of a superbubble driven by a single star cluster within the ISM. Our model does not require a continuous, globally-uniform starburst to drive outflows. One of key feature of our model is that it couples the local environment of star formation to the global effects of outflows and fountain recycling. Entropy-driven winds do not require a uniform shell to be swept up, but can rise as individual distinct bubbles through a static background CGM. Future observations may be able to distinguish between these two pictures ([Spilker et al. 2018](#)). Isolated, entropy-driven bubbles would produce a velocity distribution through the ISM with much less radial isotropy than would be produced by a global starburst.

6.3 Is the Cooling CGM Bubbly or Windy?

We have seen clearly that the stability of outflowing gas to radiative cooling will depend heavily on the mass loading in the outflow. The mass loading directly sets the initial temperature of the rising bubble, as the average bubble temperature is $T \sim (5.67 \times 10^7 \text{ K}) \eta^{-1}$, and thus the bubble's susceptibility to cooling. As was explored in ([Thompson et al. 2016](#)), a global galactic outflow powered by disc-wide SN will produce a wind roughly following the classic [Chevalier & Clegg \(1985\)](#) solution. The cooling radius of this wind, for mass loadings $\eta > 0.5$, is typically $\ll 100 \text{ kpc}$, and the cooling times are typically much less than a Hubble time. This cooling may result in a shell-like structure, where a cool shell can be accelerated and compressed out of the CGM, and may actually persist for $> \text{Gyr}$ despite this cooling, as was explored recently in ([Lochhaas et al. 2018](#)). Alternatively, this may not drive a stable, roughly spherically-symmetric set of cool shells, but instead fragment to form pressure-confined cool clouds embedded in a hot, diffuse medium ([Maller & Bullock 2004](#)), driven by [Vishniac \(1983\)](#) or similar hydrodynamic instabilities in the shocked wind. A critical difference between our approach and these previous ones is the treatment how galactic winds develop. Here, we have assumed that the fundamental unit for treating outflows are bubbles driven by individual star clusters, while ([Chevalier & Clegg 1985](#); [Thompson et al. 2016](#); [Lochhaas et al. 2018](#)) assume that disc-wide star formation drives a coherent, spherically

symmetric wind through the CGM. An interesting question for a future study is how vigorous star formation must become for bubbles driven by individual star clusters for those bubbles to merge and produce a global, uniform wind. Is the CGM best characterized as a global, spherically symmetric ([Chevalier & Clegg 1985](#)) style wind, or instead a series of convective bubbles rising and falling as high-entropy bubbles are injected and low-entropy clumps cool out? The answer will have significant consequences on the observational characteristics of the CGM absorption/emission features, as well as the overall energy budget required to maintain a quasi-stable atmosphere in L^* galaxies.

6.4 Everything Counts (in Some Amount)

The model we have presented here couples together the state of four major components of the galaxy: the ISM, the CGM, the stellar population, and the DM halo. Each of these components play a role, either in setting the initial entropy of feedback-heated gas (the density and scale height of the ISM, and the mass function of young stellar clusters), the acceleration of gas through the CGM (the entropy profile of the CGM), or the deceleration through drag or gravity (the density profile of the CGM and the DM halo). This gives us the opportunity to use this model to examine the effects of each of these on each other, and on the evolution of the galaxy as a whole.

We have interpreted the relations derived in equation 15 in terms of SN driving by a stellar cluster, but these equations are valid for any continuous injection of energy, and would lend themselves naturally to heating by AGN as well. The much higher driving luminosity of AGN ($> 10^{44} \text{ erg s}^{-1}$ [Tremmel et al. 2017](#)), as well as their potential to heat gas beyond the disc of the galaxy ([Sijacki et al. 2007](#)) means that they will be able to generate far greater entropies than SN-driven superbubbles, and produce gas that is buoyant even in cluster-mass ($\sim 10^{14} M_{\odot}$) galaxy haloes. Indeed, buoyancy is already used as a mechanism for understanding the flight of X-ray bubbles through the hot coronae of galaxy clusters ([Sanders et al. 2005](#); [Voit et al. 2017](#)).

The very weak dependence on driving luminosity that we derive in equation 15 ($K_{SB} \propto L_{38}^{2/63}$) means that even for the largest observed star clusters ($M \sim 10^7 M_{\odot}$), the entropy of gas within that cluster's superbubble will be only $\sim 30\%$ greater than that of a cluster with only 10 massive stars $M \sim 10^3 M_{\odot}$. This helps in part to explain why stellar feedback becomes ineffective above $M_{halo} \sim 10^{12} M_{\odot}$, and why AGN feedback may be required to effectively regulate the star formation and baryon content of these galaxies ([Keller et al. 2016](#); [Bower et al. 2017](#)).

6.5 Caveats and Future Work

While we have shown that this model can reproduce both observations and simulations of the CGM, and that our assumptions about the generation of entropy by feedback in the ISM are broadly in agreement with high-resolution ISM simulations, we have made a number of simplifying assumptions throughout this work.

The primary simplification we have made in developing the equations governing entropy-driven winds is the simple

1D approximation used throughout section 2. We have assumed here that both the growth of a superbubble in the ISM as well as the structure of the CGM can be approximated as radially symmetric. Furthermore, we have assumed that the of the CGM is both well-approximated by a power-law stratified entropy profile, and is in rough hydrostatic equilibrium. It is known from theoretical arguments (Nulsen 1986) and simulations (Dekel & Birnboim 2006) that galaxies are fed by cool, denser streams for much of their life, especially at high redshift $z > 1$. How entropy-driven winds may interact with these filaments will require further study. We have also modelled the mass profile of the galaxy as a singular isothermal sphere, with a rotation speed set only by the virial mass M_{200} . Further work will be needed to examine the behaviour of entropy-driven winds in different CGM profiles, as well as to examine the effects of inhomogeneous, non-radially symmetric CGM atmospheres.

In addition to the simplifications made in the geometry of the galaxy halo, we have opted here to use a very simple analytic model for the high entropy superbubble. We do not use the profile in ρ and T for the interior of the bubble derived by Weaver et al. (1977) and Mac Low & McCray (1988), but instead assume that the bubble becomes homogenized during break out and the subsequent rise through the CGM. Treating the internal structure of the bubble in a more self-consistent way would yield a spectrum of recycling/cooling times for feedback heated gas, with the hottest, most diffuse gas inside the superbubble travelling the furthest from the galaxy and recycling/cooling on the longest timescale (which would in turn set where in the CGM dust and metal-rich gas is deposited). Determining the degree to which this might result in shear-driven mixing inside the bubble, driving it towards the simple homogeneous state we assume here will require high resolution 3D simulations of both superbubble break out and its subsequent flight through the CGM. This could easily be combined with a self-consistent treatment of the cooling within this bubble, which would allow the loss of entropy through radiation to couple to the acceleration due to buoyancy. Recent simulations are beginning to reach sufficient resolution (\sim pc) to resolve this process (Kim & Ostriker 2018; Schneider & Robertson 2018).

7 CONCLUSION

In this paper, we have presented a novel theory for understanding the mechanism for accelerating outflows and fountains from galaxies, driven through hydrodynamic interactions between feedback-heated gas and the CGM. These entropy-driven winds have modest characteristic velocities ($\sim 100 \text{ km s}^{-1}$), well below the escape velocities of their parent haloes. Despite this, these outflows can spend a significant time in the CGM, depleting the galactic disc of metals and baryons, and slowing star formation by removing its fuel. As we find, the results of both cosmological simulations of L^* galaxy evolution and high-resolution simulations of superbubble growth in the ISM are in broad agreement with the predictions of this model. We also find that these entropy-driven winds well-reproduce the key observations of the CGM kinematics probed by COS-Halos (Werk et al. 2014).

Entropy-driven winds may be the key to producing galaxies with low baryon and stellar fractions, and to distributing the metals produced by star formation far from the disc of galaxies with $M_{200} \sim 10^{12}$ or below. Alternative mechanisms for launching outflows, especially simple ballistic launching after a brief, sharp injection of momentum by stellar feedback cannot produce highly mass loaded winds with sufficient velocity to reach high galactocentric radii, or to avoid re-accreting in \ll Gyr, even if hydrodynamic drag and mixing is ignored. Entropy-driven winds on the other hand, can easily reach > 100 kpc above the disc, and re-accrete in a significant fraction of a Hubble time. In more massive haloes, we have confirmed that the increased CGM entropy does suppress these outflows, as was predicted in Bower et al. (2017).

Entropy-driven winds are not new physics. They rely on simple, classical hydrodynamics (Chandrasekhar 1961; Voit et al. 2017) and the self-similar evolution of superbubbles (Weaver et al. 1977; Mac Low & McCray 1988). By taking into account the generation of entropy by feedback, and the buoyancy of feedback heated gas, we have now developed a model for the galactic baryon cycle that shows how feedback from stars, the structure of the ISM, and the stratification of the CGM couple together to determine the kinematics and timescales involved in fountain flows between the ISM and CGM. We look forward to seeing this model applied to understand the evolution of simulations and results of observations, and incorporated into future (semi-)analytic models of galaxy formation and evolution.

ACKNOWLEDGEMENTS

The analysis was performed using yt (<http://yt-project.org>, Turk et al. 2011) and pynbody (<http://pynbody.github.io/>, Pontzen et al. 2013). We thank G. Mark Voit, Jessica Werk, and S. Peng Oh for valuable conversations regarding this paper. We especially would like to thank Jessica Werk for providing data from COS-Halos and Mordecai-Mark Mac Low for pointing us towards the Hill et al. (2018b) simulations, and for the authors making their outputs available through the American Museum of Natural History Research Library Digital Repository. We also would like to thank the anonymous referee for the helpful suggestions on improving this paper. The simulations were performed on the clusters hosted on SCINET, part of ComputeCanada. We greatly appreciate the contributions of these computing allocations. We also thank NSERC for funding supporting this research. BWK and JMDK gratefully acknowledge funding from the European Research Council (ERC) under the European Union’s Horizon 2020 research and innovation programme via the ERC Starting Grant MUSTANG (grant agreement number 714907). BWK acknowledges funding in the form of a Postdoctoral Research Fellowship from the Alexander von Humboldt Stiftung. JMDK acknowledges funding from the German Research Foundation (DFG) in the form of an Emmy Noether Research Group (grant number KR4801/1-1).

REFERENCES

Agertz O., Kravtsov A. V., Leitner S. N., Gnedin N. Y., 2013, *ApJ*, **770**, 25

- Aguirre A., Hernquist L., Schaye J., Weinberg D. H., Katz N., Gardner J., 2001, *ApJ*, 560, 599
- Babyk I. V., McNamara B. R., Nulsen P. E. J., Russell H. R., Vantyghem A. N., Hogan M. T., Pulido F. A., 2018, *ApJ*, 862, 39
- Balbus S. A., Soker N., 1989, *ApJ*, 341, 611
- Behroozi P. S., Wechsler R. H., Conroy C., 2013, *ApJ*, 770, 57
- Bertone S., De Lucia G., Thomas P. A., 2007, *MNRAS*, 379, 1143
- Bouché N., Lehnert M. D., Aguirre A., Péroux C., Bergeron J., 2007, *MNRAS*, 378, 525
- Bower R. G., Schaye J., Frenk C. S., Theuns T., Schaller M., Crain R. A., McAlpine S., 2017, *MNRAS*, 465, 32
- Bregman J. N., Anderson M. E., Miller M. J., Hodges-Kluck E., Dai X., Li J.-T., Li Y., Qu Z., 2018, *ApJ*, 862, 3
- Brüggen M., Scannapieco E., Heinz S., 2009, *MNRAS*, 395, 2210
- Castor J., McCray R., Weaver R., 1975, *ApJ*, 200, L107
- Cen R., Ostriker J. P., 1999, *ApJ*, 514, 1
- Chabrier G., 2003, *PASP*, 115, 763
- Chandrasekhar S., 1961, Hydrodynamic and hydromagnetic stability
- Chevalier R. A., Clegg A. W., 1985, *Nature*, 317, 44
- Chevance M., et al., 2019, *MNRAS*, p. 3155
- Christensen C. R., Davé R., Governato F., Pontzen A., Brooks A., Munshi F., Quinn T., Wadsley J., 2016, *ApJ*, 824, 57
- Cowie L. L., McKee C. F., 1977, *ApJ*, 211, 135
- Cowie L. L., Fabian A. C., Nulsen P. E. J., 1980, *MNRAS*, 191, 399
- Crain R. A., et al., 2015, *MNRAS*, 450, 1937
- Dalla Vecchia C., Schaye J., 2008, *MNRAS*, 387, 1431
- Dalla Vecchia C., Schaye J., 2012, *MNRAS*, 426, 140
- Dalla Vecchia C., Bower R. G., Theuns T., Balogh M. L., Mazzotta P., Frenk C. S., 2004, *MNRAS*, 355, 995
- Davé R., Hellsten U., Hernquist L., Katz N., Weinberg D. H., 1998, *ApJ*, 509, 661
- Davé R., Thompson R., Hopkins P. F., 2016, *MNRAS*, 462, 3265
- Dehnen W., Binney J., 1998, *MNRAS*, 294, 429
- Dekel A., Birnboim Y., 2006, *MNRAS*, 368, 2
- Di Matteo T., Springel V., Hernquist L., 2005, *Nature*, 433, 604
- Dong R., Stone J. M., 2009, *ApJ*, 704, 1309
- El-Badry K., Ostriker E. C., Kim C.-G., Quataert E., Weisz D. R., 2019, *MNRAS*, 490, 1961
- Erb D. K., Shapley A. E., Pettini M., Steidel C. C., Reddy N. A., Adelberger K. L., 2006, *ApJ*, 644, 813
- Fall S. M., Efstathiou G., 1980, *MNRAS*, 193, 189
- Fielding D., Quataert E., Martizzi D., 2018, *MNRAS*, 481, 3325
- Finlator K., Davé R., 2008, *MNRAS*, 385, 2181
- Fryxell B., et al., 2000, *ApJS*, 131, 273
- Fukugita M., Hogan C. J., Peebles P. J. E., 1998, *ApJ*, 503, 518
- Ginsburg A., et al., 2016, *A&A*, 595, A27
- Ginsburg A., et al., 2018, *ApJ*, 853, 171
- Girichidis P., et al., 2016, *MNRAS*, 456, 3432
- Girichidis P., Naab T., Hanasz M., Walch S., 2018, *MNRAS*, 479, 3042
- Governato F., et al., 2004, *ApJ*, 607, 688
- Green J. C., et al., 2012, *ApJ*, 744, 60
- Gronke M., Peng Oh S., 2019, *MNRAS*, p. 2995
- Gupta A., Mathur S., Krongold Y., Nicastro F., Galeazzi M., 2012, *ApJ*, 756, L8
- Haardt F., Madau P., 2012, *ApJ*, 746, 125
- Hill A. S., Mac Low M.-M., Gatto A., Ibáñez-Mejía J. C., 2018a, Supplemental Data: Effect of the Heating Rate on the Stability of the Three-phase Interstellar Medium, doi:doi:10.5531/sd.astro.2, <http://digitallibrary.amnh.org/handle/2246/6888>
- Hill A. S., Mac Low M.-M., Gatto A., Ibáñez-Mejía J. C., 2018b, *ApJ*, 862, 55
- Hindmarsh A., 1982, ODEPACK, a Systematized Collection of ODE Solvers. Lawrence Livermore National Laboratory, <https://books.google.ch/books?id=9XWPmwEACAAJ>
- Hopkins P. F., Quataert E., Murray N., 2012, *MNRAS*, 421, 3522
- Hopkins P. F., Kereš D., Oñorbe J., Faucher-Giguère C.-A., Quataert E., Murray N., Bullock J. S., 2014, *MNRAS*, 445, 581
- Hudson M. J., et al., 2015, *MNRAS*, 447, 298
- Ipavich F. M., 1975, *ApJ*, 196, 107
- Jones E., Oliphant T., Peterson P., et al., 2001, SciPy: Open source scientific tools for Python, <http://www.scipy.org/>
- Joung M. K. R., Mac Low M.-M., 2006, *ApJ*, 653, 1266
- Kaiser N., 1991, *ApJ*, 383, 104
- Kaiser C. R., Pavlovski G., Pope E. C. D., Fangohr H., 2005, *MNRAS*, 359, 493
- Katz N., 1992, *ApJ*, 391, 502
- Keller B. W., Wadsley J., Benincasa S. M., Couchman H. M. P., 2014, *MNRAS*, 442, 3013
- Keller B. W., Wadsley J., Couchman H. M. P., 2015, *MNRAS*, 453, 3499
- Keller B. W., Wadsley J., Couchman H. M. P., 2016, *MNRAS*, Kim C.-G., Ostriker E. C., 2018, *ApJ*, 853, 173
- Kompaneets A. S., 1960, Soviet Physics Doklady, 5, 46
- Kruijssen J. M. D., Maschberger T., Moeckel N., Clarke C. J., Bastian N., Bonnell I. A., 2012, *MNRAS*, 419, 841
- Kruijssen J. M. D., et al., 2019, *Nature*, 569, 519
- Larson R. B., 1974, *MNRAS*, 169, 229
- Larson R. B., 1981, *MNRAS*, 194, 809
- Leitherer C., et al., 1999, *ApJS*, 123, 3
- Leroy A. K., et al., 2015, *ApJ*, 814, 83
- Li M., Bryan G. L., Ostriker J. P., 2017, *ApJ*, 841, 101
- Lochhaas C., Thompson T. A., Quataert E., Weinberg D. H., 2018, *MNRAS*, 481, 1873
- Loewenstein M., 1989, *MNRAS*, 238, 15
- Longmore S. N., et al., 2014, in Beuther H., Klessen R. S., Dullemond C. P., Henning T., eds, Protostars and Planets VI. p. 291 ([arXiv:1401.4175](https://arxiv.org/abs/1401.4175)), doi:10.2458/azu_uapress_9780816531240-ch013
- Ma X., Hopkins P. F., Faucher-Giguère C.-A., Zolman N., Muratov A. L., Kereš D., Quataert E., 2016, *MNRAS*, 456, 2140
- Mac Low M.-M., McCray R., 1988, *ApJ*, 324, 776
- Maller A. H., Bullock J. S., 2004, *MNRAS*, 355, 694
- Marasco A., Fraternali F., Binney J. J., 2012, *MNRAS*, 419, 1107
- Martin C. L., Kobulnicky H. A., Heckman T. M., 2002, *ApJ*, 574, 663
- McCourt M., O’Leary R. M., Madigan A.-M., Quataert E., 2015, *MNRAS*, 449, 2
- McNamara B. R., Nulsen P. E. J., 2007, *ARAA*, 45, 117
- McNamara B. R., Nulsen P. E. J., Wise M. W., Rafferty D. A., Carilli C., Sarazin C. L., Blanton E. L., 2005, *Nature*, 433, 45
- Mitchell P. D., Schaye J., Bower R. G., Crain R. A., 2019, arXiv e-prints, p. [arXiv:1910.09566](https://arxiv.org/abs/1910.09566)
- Mok A., Chandar R., Fall S. M., 2019, *ApJ*, 872, 93
- Morganti R., Oosterloo T. A., Emons B. H. C., van der Hulst J. M., Tadhunter C. N., 2003, *ApJ*, 593, L69
- Moster B. P., Naab T., White S. D. M., 2013, *MNRAS*, 428, 3121
- Munshi F., et al., 2013, *ApJ*, 766, 56
- Muratov A. L., Kereš D., Faucher-Giguère C.-A., Hopkins P. F., Quataert E., Murray N., 2015, *MNRAS*, 454, 2691
- Murray N., Quataert E., Thompson T. A., 2010, *ApJ*, 709, 191
- Murray N., Ménard B., Thompson T. A., 2011, *ApJ*, 735, 66
- Nicastro F., et al., 2018, *Nature*, 558, 406
- Nulsen P. E. J., 1986, *MNRAS*, 221, 377
- Omma H., Binney J., Bryan G., Slyz A., 2004, *MNRAS*, 348, 1105
- Oppenheimer B. D., Davé R., 2008, *MNRAS*, 387, 577
- Papastergis E., Cattaneo A., Huang S., Giovanelli R., Haynes M. P., 2012, *ApJ*, 759, 138
- Peebles M. S., Shankar F., 2011, *MNRAS*, 417, 2962

- Peebles M. S., Werk J. K., Tumlinson J., Oppenheimer B. D., Prochaska J. X., Katz N., Weinberg D. H., 2014, *ApJ*, **786**, 54
- Planck Collaboration et al., 2014, *A&A*, **571**, A16
- Pontzen A., Governato F., 2012, *MNRAS*, **421**, 3464
- Pontzen A., Roškar R., Stinson G., Woods R., 2013, pynbody: N-Body/SPH analysis for python, Astrophysics Source Code Library (ascl:1305.002)
- Press W. H., Schechter P., 1974, *ApJ*, **187**, 425
- Prochaska J. X., et al., 2017, *ApJ*, **837**, 169
- Putman M. E., Peek J. E. G., Jounge M. R., 2012, *ARAA*, **50**, 491
- Quilis V., Bower R. G., Balogh M. L., 2001, *MNRAS*, **328**, 1091
- Raymond J. C., Cox D. P., Smith B. W., 1976, *ApJ*, **204**, 290
- Rees M. J., Ostriker J. P., 1977, *MNRAS*, **179**, 541
- Sanders J. S., Fabian A. C., Dunn R. J. H., 2005, *MNRAS*, **360**, 133
- Sarkar K. C., Nath B. B., Sharma P., Shchekinov Y., 2015, *MNRAS*, **448**, 328
- Scannapieco E., Brüggem M., 2015, *ApJ*, **805**, 158
- Scannapieco C., et al., 2012, *MNRAS*, **423**, 1726
- Schneider E. E., Robertson B. E., 2018, *ApJ*, **860**, 135
- Shen S., Wadsley J., Stinson G., 2010, *MNRAS*, **407**, 1581
- Sijacki D., Springel V., Di Matteo T., Hernquist L., 2007, *MNRAS*, **380**, 877
- Smith B. D., et al., 2017, *MNRAS*, **466**, 2217
- Somerville R. S., Primack J. R., 1999, *MNRAS*, **310**, 1087
- Songaila A., Cowie L. L., 1996, *AJ*, **112**, 335
- Spilker J. S., et al., 2018, *Science*, **361**, 1016
- Spitzer Jr. L., 1956, *ApJ*, **124**, 20
- Springel V., Hernquist L., 2003, *MNRAS*, **339**, 289
- Steidel C. C., Erb D. K., Shapley A. E., Pettini M., Reddy N., Bogosavljević M., Rudie G. C., Rakic O., 2010, *ApJ*, **717**, 289
- Stinson G. S., Bailin J., Couchman H., Wadsley J., Shen S., Nickerson S., Brook C., Quinn T., 2010, *MNRAS*, **408**, 812
- Stocke J. T., Keeney B. A., Danforth C. W., Shull J. M., Froning C. S., Green J. C., Penton S. V., Savage B. D., 2013, *ApJ*, **763**, 148
- Thompson T. A., Quataert E., Zhang D., Weinberg D. H., 2016, *MNRAS*, **455**, 1830
- Tremmel M., Karcher M., Governato F., Volonteri M., Quinn T. R., Pontzen A., Anderson L., Bellovary J., 2017, *MNRAS*, **470**, 1121
- Tumlinson J., et al., 2011, *Science*, **334**, 948
- Tumlinson J., et al., 2013, *ApJ*, **777**, 59
- Turk M. J., Smith B. D., Oishi J. S., Skory S., Skillman S. W., Abel T., Norman M. L., 2011, *The Astrophysical Journal Supplement Series*, **192**, 9
- Vishniac E. T., 1983, *ApJ*, **274**, 152
- Voit G. M., Meece G., Li Y., O'Shea B. W., Bryan G. L., Donahue M., 2017, *ApJ*, **845**, 80
- Voit G. M., Donahue M., Zahedy F., Chen H.-W., Werk J., Bryan G. L., O'Shea B. W., 2019, *ApJ*, **879**, L1
- Walch S. K., Whitworth A. P., Bisbas T., Wünsch R., Hubber D., 2012, *MNRAS*, **427**, 625
- Weaver R., McCray R., Castor J., Shapiro P., Moore R., 1977, *ApJ*, **218**, 377
- Werk J. K., et al., 2014, *ApJ*, **792**, 8
- Werk J. K., et al., 2016, *ApJ*, **833**, 54
- Werner N., Allen S. W., Simionescu A., 2012, *MNRAS*, **425**, 2731
- White S. D. M., Rees M. J., 1978, *MNRAS*, **183**, 341
- Zhao D. H., Mo H. J., Jing Y. P., Börner G., 2003, *MNRAS*, **339**, 12
- van de Voort F., Quataert E., Hopkins P. F., Faucher-Giguère C.-A., Feldmann R., Kereš D., Chan T. K., Hafen Z., 2016, *MNRAS*, **463**, 4533